LEVEL II

12

VSC-TR-81-21

SEISMOLOGICAL DISCRIMINATION AND
YIELD DETERMINATION RESEARCH

VELA SEISMOLOGICAL CENTER

FINAL REPORT
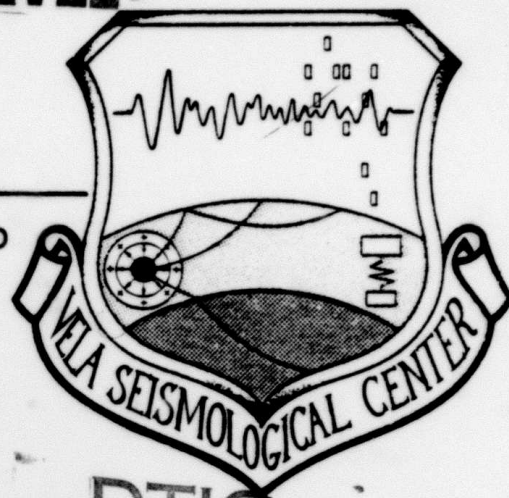
DTIC
SELECTED
NOV 1 0 1981
E
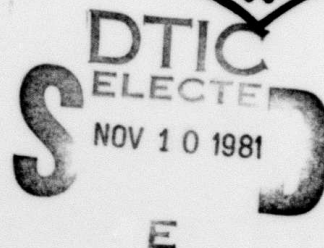
SYSTEMS, SCIENCE AND SOFTWARE
P.O. Box 1620
La Jolla, California 92038

June 1981

APPROVED FOR PUBLIC RELEASE,
DISTRIBUTION UNLIMITED

Monitored By:

VELA Seismological Center
312 Montgomery Street
Alexandria, VA 22314

81 11 09 025

REPORT DOCUMENTATION PAGE

1. REPORT NUMBER	2. GOVT ACCESSION NO.	3. RECIPIENT'S CATALOG NUMBER
VSC-TR-81-21	AD-A107360	

4. TITLE (and Subtitle)

SEISMOLOGICAL DISCRIMINATION AND YIELD DETERMINATION RESEARCH

5. TYPE OF REPORT & PERIOD COVERED

Final Report
9/30/79 - 9/30/80

6. PERFORMING ORG. REPORT NUMBER

SSS-R-81-5033

7. AUTHOR(s)

T. C. Bache, T. G. Barker, N. Rimer, J. T. Cherry, W. E. Farrell, R. C. Goff, J. Wang, J. Berger, B. Shkoller, (continued)

8. CONTRACT OR GRANT NUMBER(s)

F08606-79-C-0008

9. PERFORMING ORGANIZATION NAME AND ADDRESS

Systems, Science and Software
P. O. Box 1620
La Jolla, California 92038

10. PROGRAM ELEMENT, PROJECT, TASK AREA & WORK UNIT NUMBERS

Program Code No. 6H189
ARPA Order No. 2551

11. CONTROLLING OFFICE NAME AND ADDRESS

VELA Seismological Center
312 Montgomery Street
Alexandria, Virginia 22314

12. REPORT DATE

June 1981

13. NUMBER OF PAGES

85

14. MONITORING AGENCY NAME & ADDRESS(if different from Controlling Office)

15. SECURITY CLASS. (of this report)

Unclassified

15a. DECLASSIFICATION/DOWNGRADING SCHEDULE

16. DISTRIBUTION STATEMENT (of this Report)

Approved for Public Release, Distribution Unlimited.

Final rept. 30 Sep 79 - 30 Sep 80

17. DISTRIBUTION STATEMENT (of the abstract entered in Block 20, if different from Report)

18. SUPPLEMENTARY NOTES

19. KEY WORDS (Continue on reverse side if necessary and identify by block number)

Seismic waves   Detection
Acoustic waves   Discrimination
Earthquakes
Nuclear explosion

20. ABSTRACT (Continue on reverse side if necessary and identify by block number)

This report summarizes work conducted by Systems, Science and Software concerning the generation, propagation, detection and analysis of seismic waves by both nuclear explosions and earthquake sources. Specific topics covered included numerical simulation of the near field ground motion from earthquakes and explosions, automatic signal processing relating to the detection of seismic events and magnitude determination, a compilation of near

7. Authors (continued)

J. R. Murphy, T. J. Bennett, M. G. Brown, K. D. Pyatt and
H. J. Swanger

contd

20. Abstract (continued)

source data and the synthesis of this data in terms of the
seismic source function, and the determination of the spec-
tral characteristics of acoustic waves from an explosion
near the ocean surface.

AFTAC Project Authorization No. VT/0712/B/PMP

ARPA Order No. 2551, Program Code No. 6H189

Effective Date of Contract: November 17, 1978

Contract Expiration Date: November 15, 1981

Amount of Contract: $1,816,437

Contract No. F08606-79-C-0008

Principal Investigator and Phone No.
    Dr. J. Theodore Cherry, (714) 453-0060

Project Scientist and Phone No.
    Mr. Brian W. Barker, (202) 325-7581

The views and conclusions contained in this document are those of the authors and should not be interpreted as necessarily representing the official policies, either expressed or implied, of the Advanced Research Projects Agency, the Air Force Technical Applications Center, or the U.S. Government.

TABLE OF CONTENTS

i

TABLE OF CONTENTS (continued)

TABLE OF CONTENTS (continued)

LIST OF ILLUSTRATIONS

LIST OF ILLUSTRATIONS (continued)

LIST OF ILLUSTRATIONS (continued)

I. INTRODUCTION AND SUMMARY

1.1 INTRODUCTION

The objective of the Systems, Science and Software (S³) research program is to extend our present understanding of the generation, propagation, detection and analysis of seismic waves by both underground explosions and earthquake sources. The goal is to improve the United States' ability to monitor compliance with treaties limiting underground nuclear explosions. This report covers work performed at S³ during the twelve month contract period between 1 October 1979 and 1 October 1980, under Contract Number F08606-79-C-0008 (VSC Project VT/0712).

The report includes six distinct technical sections, which are briefly summarized below, together with the references to the appropriate task in the Work Statement of the contract. Much of this work has been described previously in several S³ topical and technical reports. In such cases, we have provided an executive summary of the work performed during the contract period, including a digest of the principal conclusions and the relevant figures.

1.2 SUMMARY OF SECTION II: SEISMIC SOURCE CALCULATIONS

This section contains three subsections.

- Development of a constitutive model for salt based on an analysis of free-field ground motion data for nuclear and high explosive events in salt. The events included GNOME, SALMON, STERLING and COWBOY. Because of the large body of digitized data available for SALMON, this event was chosen for normalization purposes. The purpose was to explain

1

simultaneously all observations with a single
constitutive model for salt so as to permit
development of realistic decoupling scenarios.
Good agreement with data from STERLING and
GNCME was produced. For COWBOY, predicted
and observed peak velocities were in agree-
ment, but predicted peak displacements were
larger than those observed by a factor of
two. This work was done by Dr. J. Theodore
Cherry and Dr. Norton Rimer.

- Analysis of the dynamical aspects of seismic
  sources which yield different signatures for
  earthquakes and explosions was conducted through
  numerical simulations of earthquake sources.
  The simulations were performed on the ILLIAC IV
  computer, using a three-dimensional finite
  difference code. Inelastic response along the
  fault zone was modeled through nonlinear boundary
  conditions on the fault plane. As a result of
  this work, it appears necessary to include more
  complex rupture physics in the modeling procedure,
  and, in particular, a better description of the
  cessation of rupture is required to explain the
  discrepancies between modeled and observed
  stopping phases. Stress irregularities have
  been shown to have a significant influence on
  the spectral- and time-domain characteristics
  of the teleseismic signals from earthquakes; they
  tend to increase the separation of earthquake and
  explosion populations for the m_b-M_s discriminant.
  This work was performed by Dr. Steven M. Day.

2

- A simulation study for a (hypothetical) fully
  decoupled 5.3 KT explosion at the SALMON site
  was conducted by scaling regional phases re-
  corded in the eastern United States for SALMON.
  Such an event could probably be detected at
  epicentral distances up to $\sim$ 650 km, but not
  at distances greater than $\sim$ 1000 km. For low-
  noise conditions, the Lg phase would probably
  be detected at distances up to $\sim$ 1500 km, but
  not the initial P phase. This study was per-
  formed by Mr. John R. Murphy and Dr. T. Joseph
  Bennett.

1.3 SUMMARY OF SECTION III: REGIONAL SEISMOLOGY

This section pertains to a study of far-field seismic
waves associated with a series of two-dimensional calculations
of buried explosions. The purpose was to determine the impor-
tance of nonlinear free surface interactions, including spalla-
tion, and the depth dependence of overburden pressure and
rheology. These effects result in higher order source prop-
erties, which constitute a departure from the classical
spherically symmetric point source approximation. This work
has been the subject of a detailed report by Drs. Thomas C.
Bache, Terrance G. Barker, Norton Rimer and J. Theodore Cherry
(1980) and we only include the executive summary for complete-
ness.

1.4 SUMMARY OF SECTION IV: AUTOMATIC SIGNAL PROCESSING

This section includes two subsections.

- A review of the MARS (Multiple Arrival
  Recognition System) detector. The MARS-
  based detection algorithm was optimized

3

and an efficient code was tested on an off-line
basis on data supplied by VELA Seismological
Center (VSC). This subsection was written by
Dr. William E. Farrell, Mr. Robert C. Goff and
Mr. James Wang.

● A review of state-of-the-art detection algorithms,
by Dr. Jonathon Berger. This section identifies
and evaluates all pertinent automatic detection
algorithms, and provides a classification by
equation, mathematical derivation, and usage
history. It includes algorithms currently under
development and scheduled to be validated by
October 1981. In addition, recommendations for
further research efforts are made.

1.5   SUMMARY OF SECTION V: EVALUATION OF SUITES OF EVENTS

This section summarizes work by Dr. Thomas C. Bache
and Mr. Boris Shkoller which is described more fully in a
semiannual technical report by Bache, et al. (1980). It
pertains to the automatic determination of body wave magni-
tudes using the MARS processor, and the testing of a similar
automatic surface wave magnitude estimator. Particular atten-
tion is paid to the effect of seismic noise, which are evalu-
ated by superposition of a signal with known magnitude and
seismic noises of varying levels. The results appear to be
robust with respect to noise even in the case of high noise
level.

Applications to actual records from Eurasian events at
RKON have also been performed and have been described in the
aforementioned report.

4

1.6   SUMMARY OF SECTION VI: GROUND MOTION ANALYSIS

This work, by Mr. John R. Murphy and Dr. T. Joseph
Bennett pertains to the compilation and evaluation of near-
source data from underground explosions. In particular, an
assessment of the data set in terms of the seismic source
function for different emplacement media has been conducted.
The expanded data set includes previously unpublished data
from the Sandia Corporation archives. A detailed report has
been provided by Murphy and Bennett (1980).

1.7   SUMMARY OF SECTION VII: ACOUSTIC WAVES FROM
        EXPLOSIONS IN THE OCEAN

The results for this section have been reported by
Bache, et al. (1980). They specifically include estimates
of the gross spectral characteristics and signal duration of
acoustic waves generated by a nuclear explosion near the
ocean surface. A nominal yield of 1 KT and nominal range of
6600 cm are assumed.

II. SEISMIC SOURCE CALCULATIONS

2.1 INTRODUCTION

Investigations of seismic sources by theoretical and numerical calculations were covered by three tasks:

One- and two-dimensional explosion calculations (Task 4.1.1). (See also Section II, Task 4.2.)

Earthquake simulation studies using the ILLIAC IV (Task 4.1.2).

Decoupling-evasion research (Task 4.1.3).

Progress accomplished under these tasks during the contract period is described in the following subsections, where specific references are made to reports in which greater detail can be found.

2.2 A CONSTITUTIVE MODEL FOR SALT BY J. T. CHERRY AND N. RIMER

Several numerical calculations of underground explosions performed at S^3 have been used principally in Task 4.2, and the results are summarized in Section II of this report.

In this subsection, we focus on calculations designed to permit development of realistic decoupling scenarios in salt. For this purpose, it is necessary to understand free field motion data for actual explosions in this material. We have used ground motion data from nuclear and high explosive events including GNOME, SALMON, STERLING and COWBOY.

Because the SALMON event provided a large subset of the data, and because many of the associated records are available in digital form, we chose this event for the purpose of normalizing the constitutive model. This model was then applied to the other events, in order to determine how much

6

of the salt ground motion observations could be explained using a single constitutive model.

This procedure produced good agreement with the ground motion data from STERLING and GNOME. The predicted peak displacements for the tamped COWBOY shots were approximately a factor of two greater than those observed. However, predicted and observed peak velocities for COWBOY were in close agreement.

2.2.1 Normalization to SALMON

Figure 1 shows the laboratory strength data for SALMON, GNOME and polycrystalline salt. The curve shown in the figure fits the data for SALMON and GNOME and was used in the model for the ultimate strength of salt (Y_{lim}).

The best agreement with the SALMON ground motion data was obtained by assuming that salt work hardened to its ultimate strength. The expression used to calculate the strength (Y) as a function of the inelastic energy (E) deposited in the material during yielding was

$$Y = Y_0(1 + e_1 E - e_2 E^2) \leq Y_{lim} \qquad (1)$$

where Y_0 is the initial (saturated) strength and e_1 and e_2 are respectively work hardening and work softening material constants.

If S_{ij} is the deviatoric component of the stress tensor and J_2' is the unadjusted second deviatoric invariant, then the increment in inelastic energy becomes

$$\Delta E = S_{ij} \, \Delta \pi_{ij} = \frac{S_{ij} \, S_{ji}}{2\mu} \, \frac{\sqrt{3J_2'} - Y}{Y} \qquad (2)$$

7
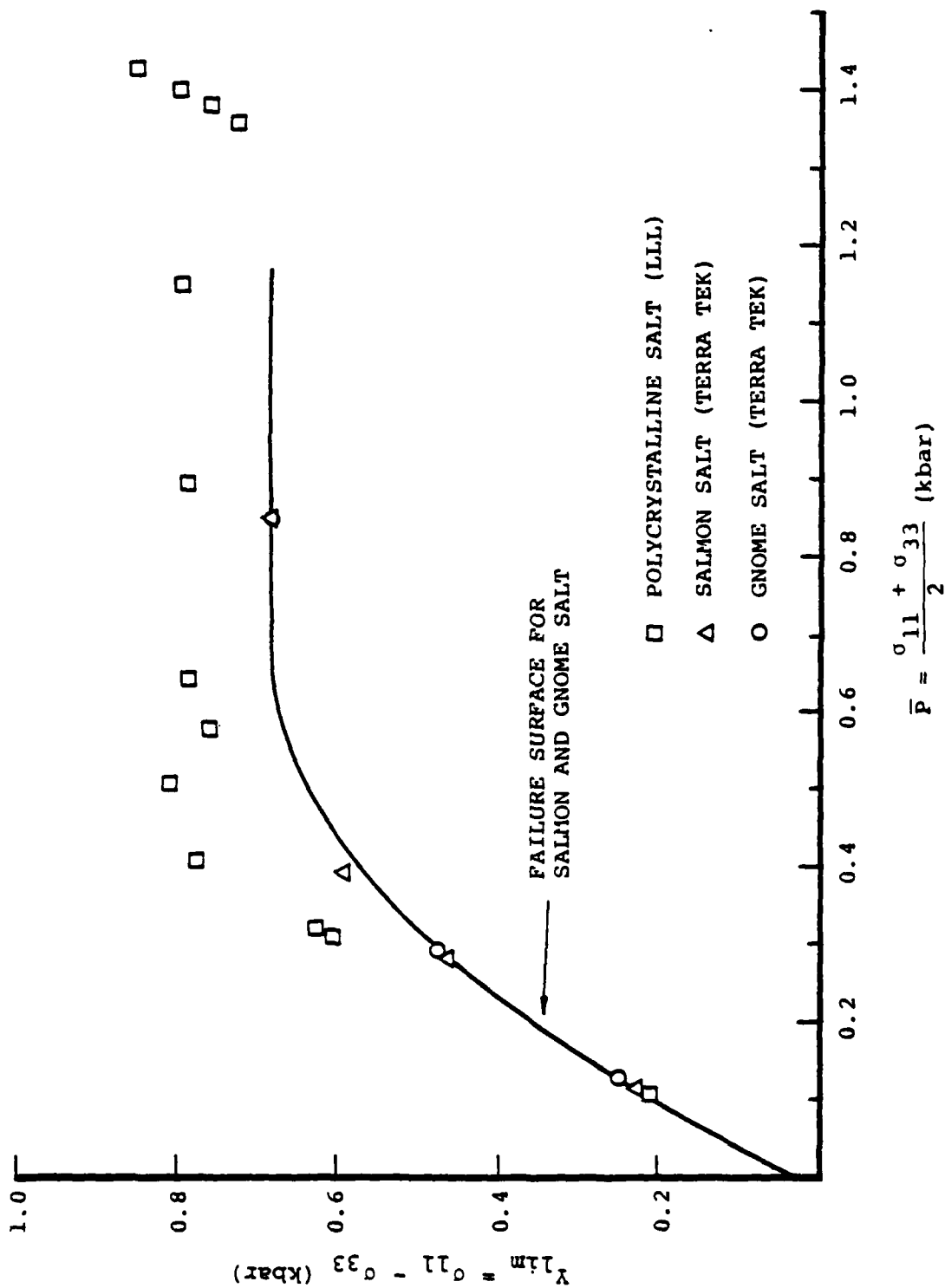
Figure 1. Strength data for salt.

$$\bar{P} = \frac{\sigma_{11} + \sigma_{33}}{2} \text{ (kbar)}$$

□ POLYCRYSTALLINE SALT (LLL)

△ SALMON SALT (TERRA TEK)

○ GNOME SALT (TERRA TEK)

FAILURE SURFACE FOR
SALMON AND GNOME SALT

$Y_{11m} = \sigma_{11} - \sigma_{33}$ (kbar)

8

where

$$3 J_2' > Y^2$$

π_{ij} = the deviatoric component of the inelastic strain tensor

μ = the shear modulus.

This model is simple and easily implemented in a finite difference stress wave code. The physical basis for the work hardening aspect of the model may be an increase in effective stress, and conversely a decrease in pore fluid pressure, caused by dilatancy. If this is the case, then Y_0 is the saturated material strength. During shock loading microcracks open, the pore fluid pressure decreases and the strength increases. During release, the cracks close, pore fluid pressure increases and strength decreases. These modes of material behavior are quantitatively contained in the model with the rate of hardening and softening determined by the constants e_1 and e_2.

Figure 2 compares the calculated and observed ground motion from SALMON at a range of 620 m where the calculations were performed with the work hardening model. The emergence of a precursor with a peak velocity of approximately 0.5 m/s is adequately modeled by assuming a saturated strength (Y_0) of 25 bars. Work hardening is required in order to match the observed pulse shape. At a radius of 967 m, the peak velocity in the calculation is determined by the precursor. Elastic material behavior occurs beyond this radius in the calculation.

Figure 3 compares calculated and observed peak velocities and peak displacements. The results of two calculations are shown in this figure; one (dashed curve) in which Y_{lim} equaled the maximum strength (0.68 kb) given in Figure 1, and

9

SALMON E11-27URH   SALT RUN 512

LAGRANGIAN POSITION 6.1987+004 CM
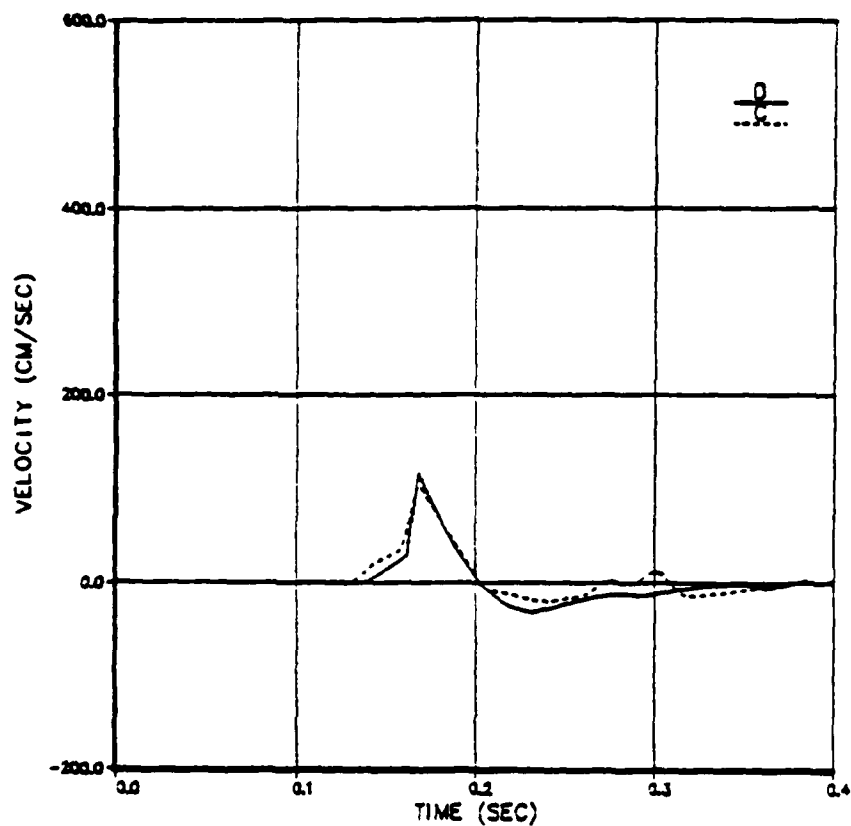
Figure 2.   Comparison between calculated (dashed curve) and
            observed (solid curve) ground motion from SALMON
            at a range of 620 m.

10
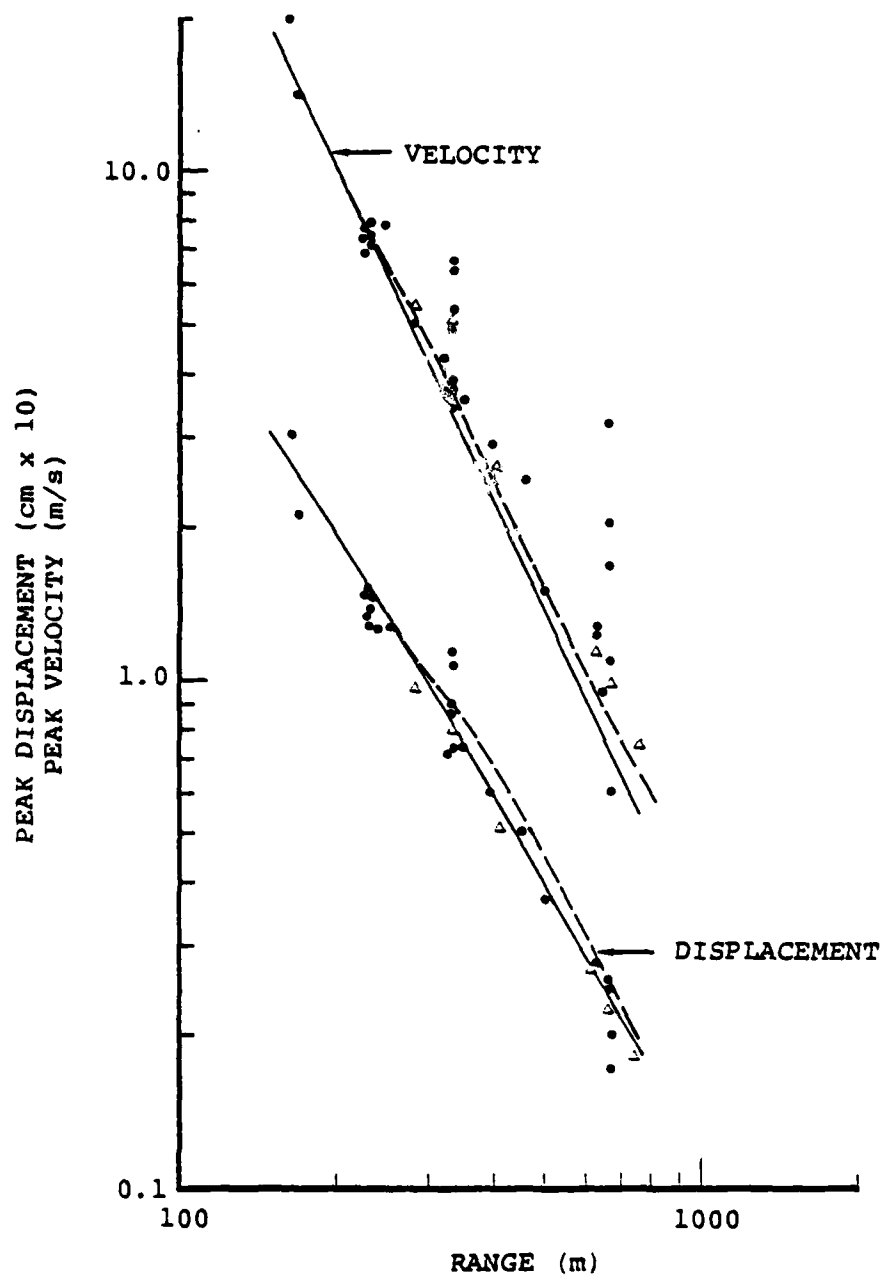
Figure 3. Comparison between calculated and observed
           peak velocities and displacements for SALMON.

11

the second (solid curve) in which Y_{lim} varied with stress state ($\overline{P}$) as shown in Figure 1.

Figure 4 shows the RVP spectra ($|\hat{\Psi}|$) for these two calculations. Also shown are the spectra of Springer, et al. (1968), which represents an average of the free field SALMON data, and Murphy, which was obtained by scaling the spectrum of the GNOME event to the yield and depth of SALMON.

These results, involving comparisons between calculated and observed ground motions and RVP spectra indicate that the constitutive model adequately explains the SALMON data. We now apply this model to other salt events.

2.2.2 STERLING

Simulation of the STERLING event was accomplished by detonating 0.38 KT in the SALMON cavity. The RVP spectrum for STERLING was calculated and divided into the calculated SALMON spectra shown in Figure 4 ($Y_{lim} = Y_{max}$). The resulting spectral ratios are shown in Figure 5. In this figure we also show the averaged spectral ratios obtained by Springer, et al. (1968) from seismic stations common to the two shots. Agreement is excellent over the frequency range analyzed by these investigators.

2.2.3 GNOME

The GNOME event was simulated using the work hardening model. Figures 6 and 7 compare calculated and observed peak velocities and displacements for this event. The calculated elastic radius was 790 m.

Figure 8 compares the Mueller-Murphy estimate of the GNOME RVP spectrum with the calculated spectrum. Agreement is surprisingly good considering that the Mueller-Murphy spectrum was based on ground motion data at a range of 300 m, a distance well within the region of nonlinear material behavior.

12
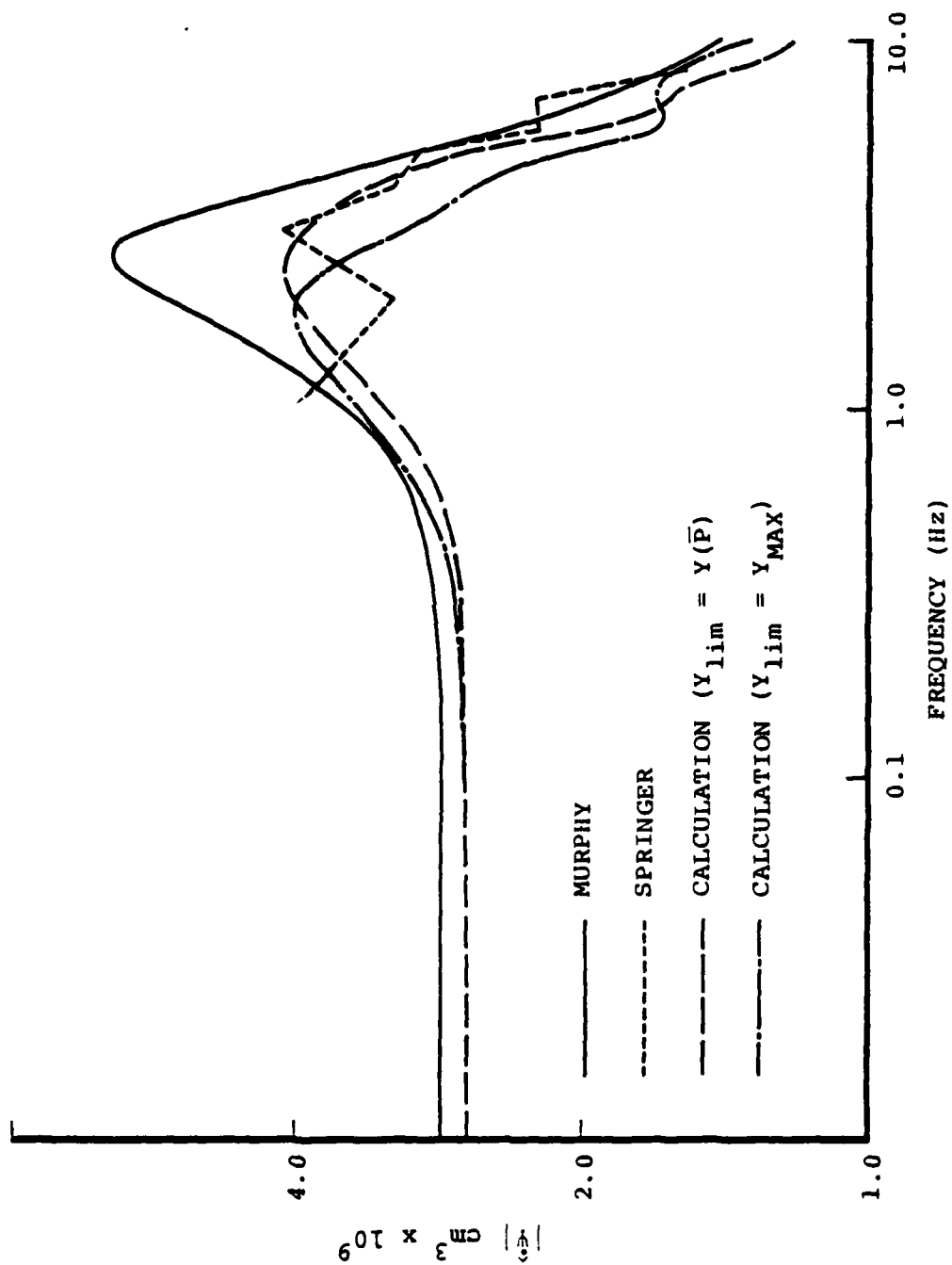
Figure 4. Comparison of calculated and observed RVP spectra for SALMON.

13
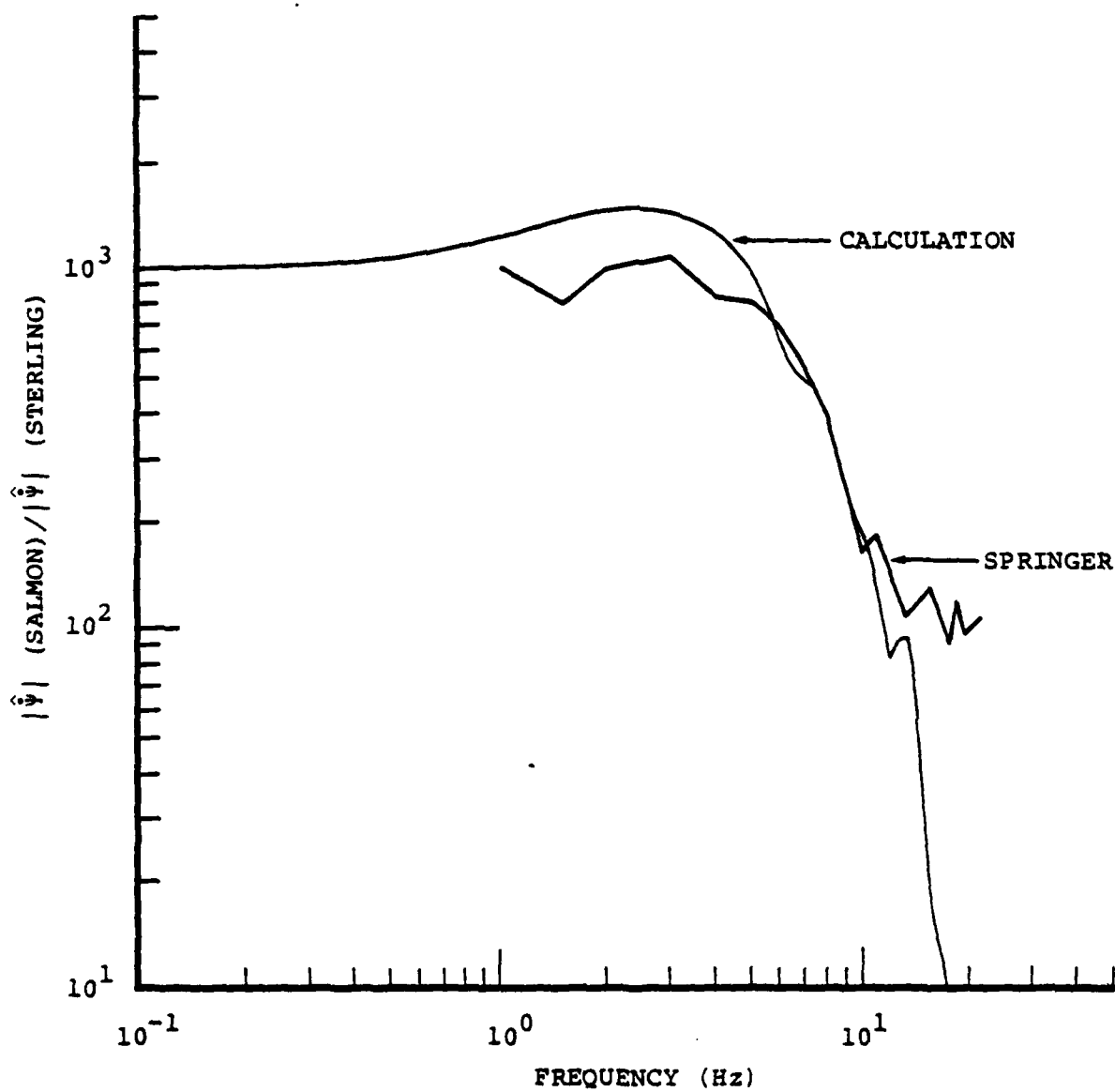
Figure 5.   Calculated and observed spectral ratios for
SALMON/STERLING.

14
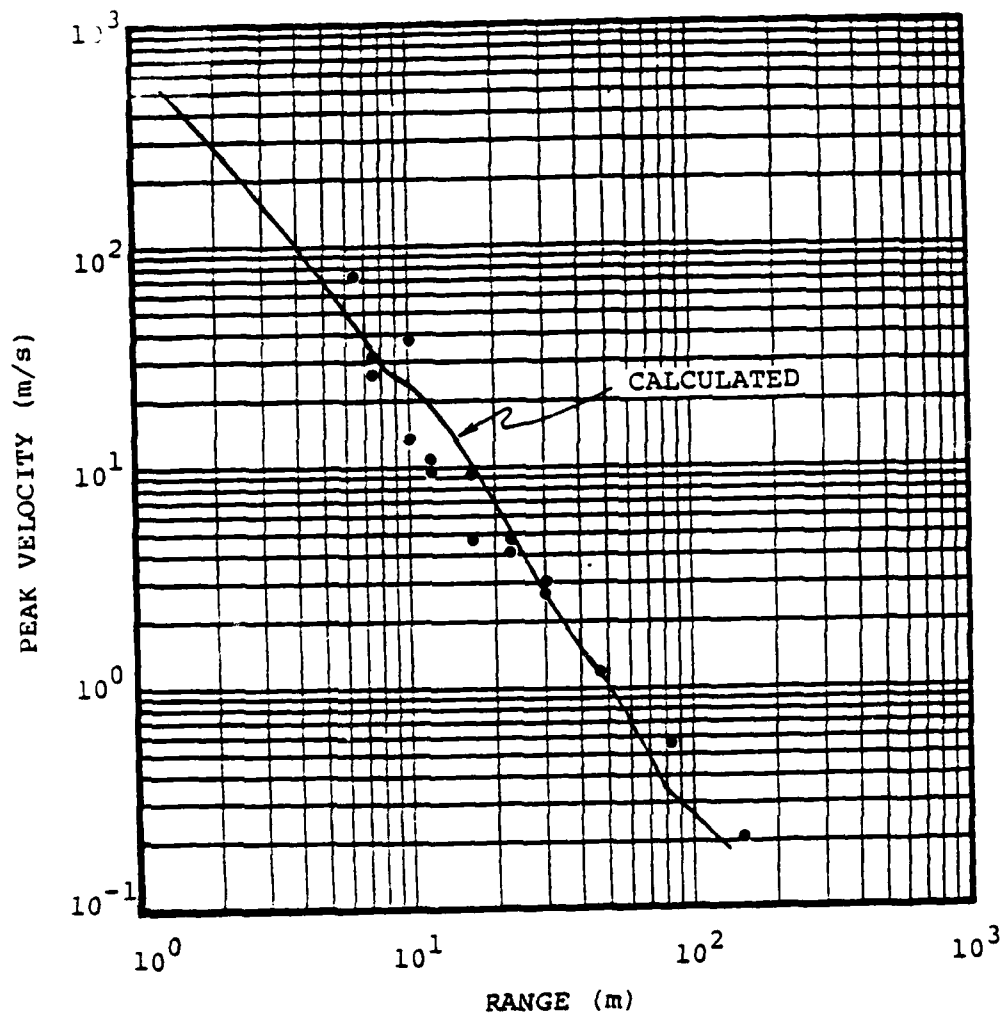
GNOME 563

Figure 6. Comparison of calculated and observed peak velocities for the GNOME event.

15

GNOME 563
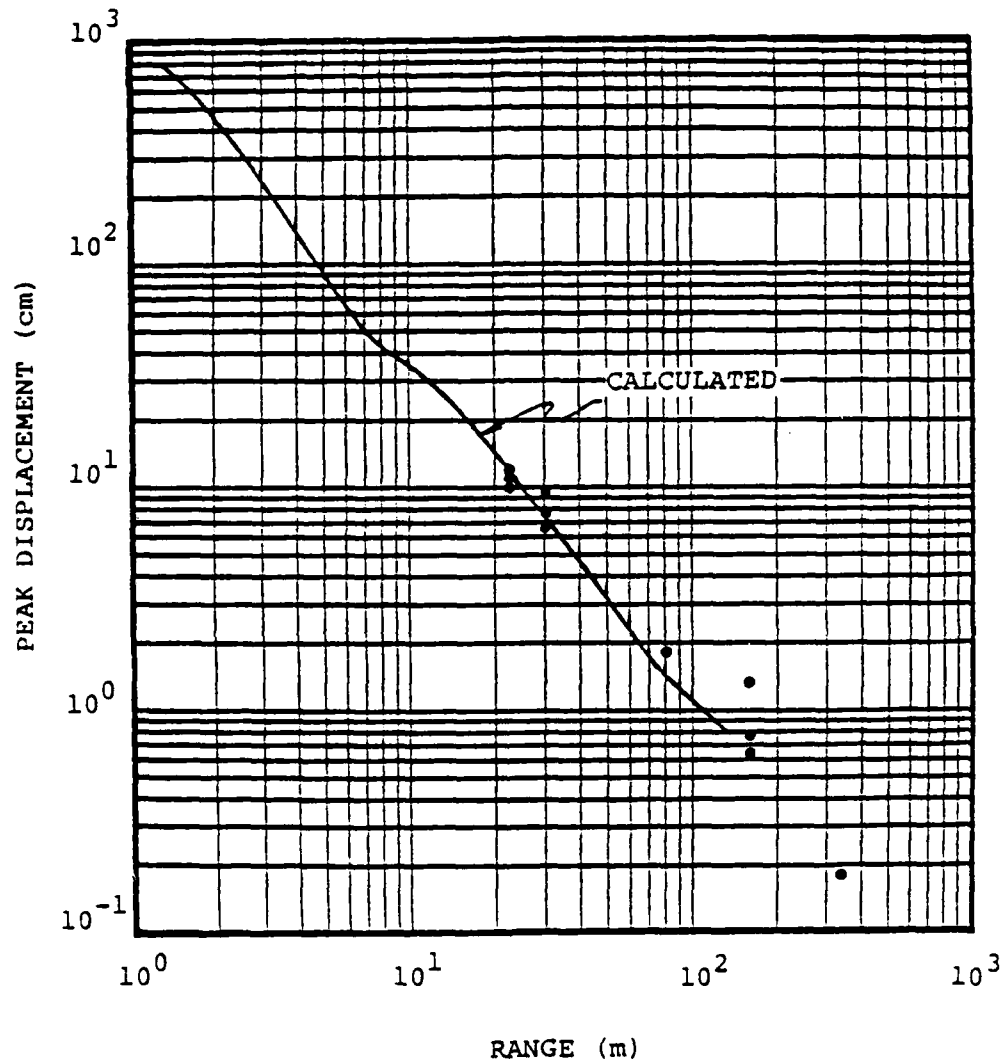
Figure 7. Comparison of calculated and observed peak displacements for the GNOME event.

16
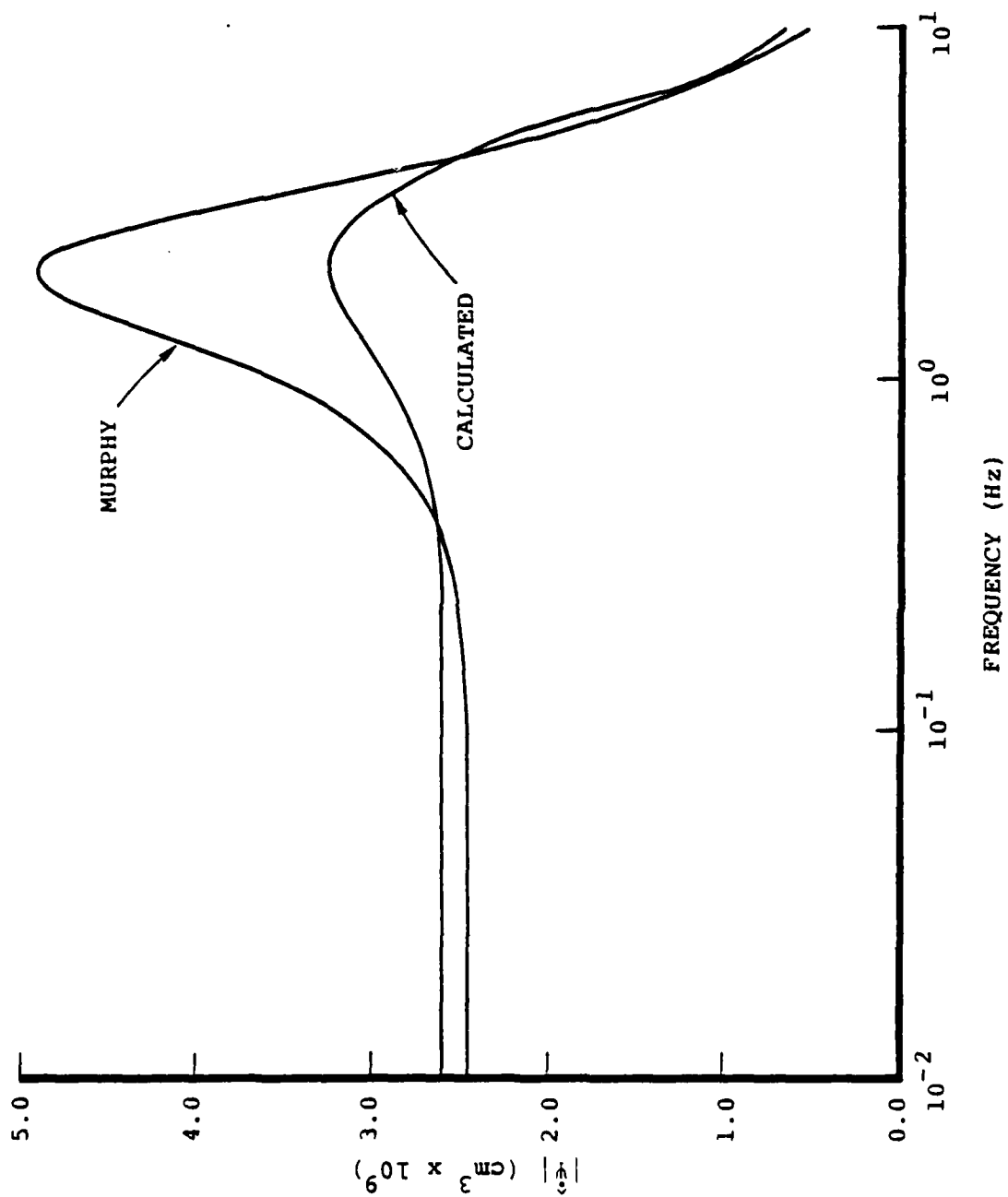
Figure 8. Comparison of calculated and observed RVP spectra for GNOME.

17

2.2.4 COWBOY

Figures 9 and 10 compare calculated and observed peak velocities and peak displacements for the tamped shots in the COWBOY series. Agreement is good for peak velocities. However, the calculated peak displacements are a factor of two larger than those observed.

There are a number of possible explanations for this result, e.g., the COWBOY salt was not saturated, the HE was not adequately simulated, the peak displacements were not free field, the charge emplacement was not consistent with a spherically symmetric geometry, the material properties (strength and wave velocities) of the COWBOY salt are different from GNOME and SALMON.

These issues are worth pursuing, but not here. Our objective was to develop a constitutive model for salt based on SALMON ground motion data and then to determine its range of applicability for other salt events. The results of the model are consistent with data from STERLING and GNOME. They are not consistent with the data from the tamped COWBOY series.

2.3 EARTHQUAKE SIMULATION STUDIES USING THE ILLIAC IV BY S. M. DAY

Differentiation of earthquakes from underground nuclear explosions on the basis of their seismic signatures ultimately depends on features related to the details of source dynamics. We have conducted a series of numerical calculations on the ILLIAC IV computer designed to provide a realistic three-dimensional model of the earthquake rupture phenomenon. These are dynamical simulations, which can be compared in turn with simple elastostatic or kinematical solutions in order to help identify the effect of rupture complexities on the observable seismograms. This research has been previously reported by Bache, et al. (1980a).

18
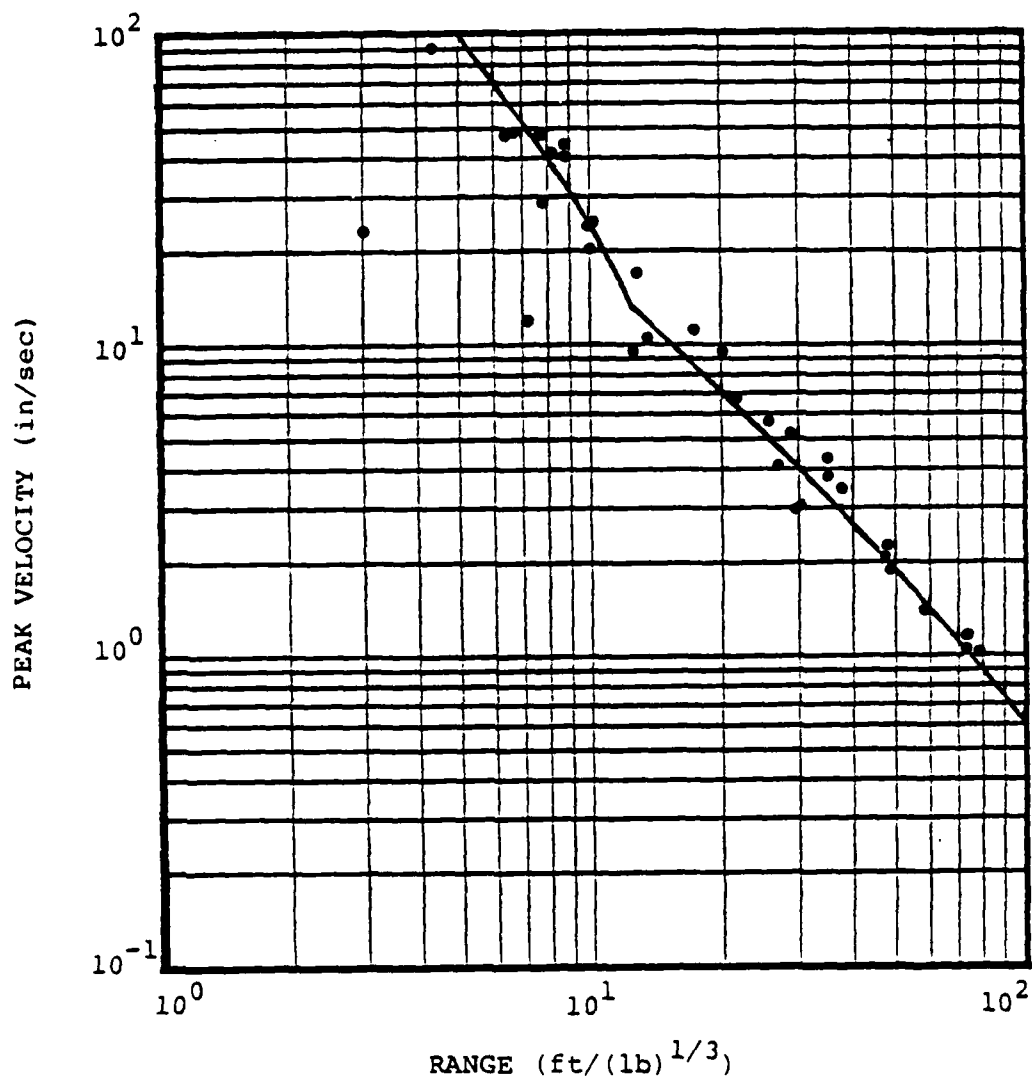
Figure 9. Comparison of observed and calculated peak
velocities for the tamped COWBOY events.

19
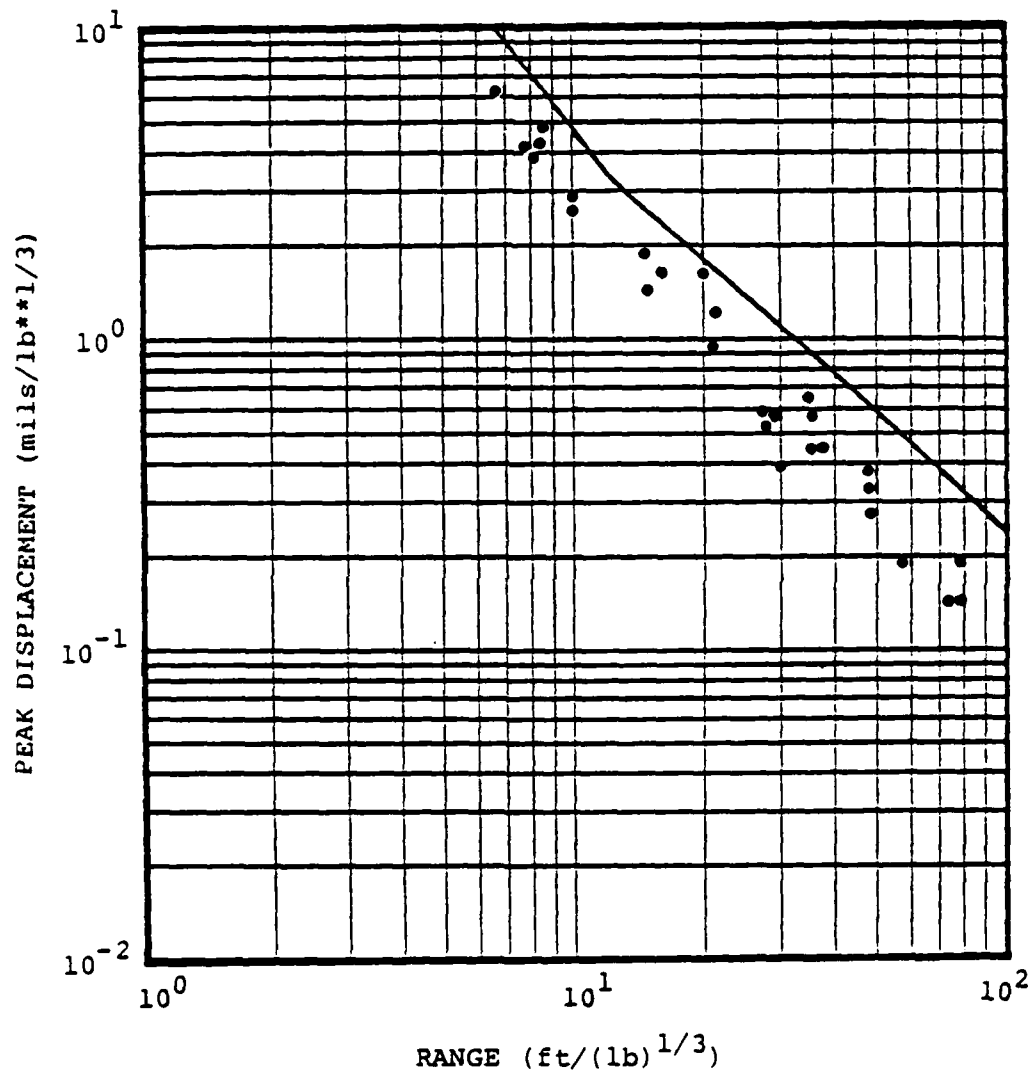
Figure 10.   Comparison of observed and calculated peak
displacements for the tamped COWBOY events.

20

We are using a three-dimensional finite difference method to model the features of earthquake dynamics believed to be important for predicting the teleseismic signal. The calculations have simulated inelastic response of the fault zone through nonlinear boundary conditions on the fault plane. The numerical method admits more general nonlinear material behavior, which is being incorporated as required.

Our initial numerical simulations were for a simple, constant rupture velocity, constant stress-drop earthquake model. These results show a significant influence of fault width on the slip function. For points on the fault which are more than a fault width away from the focus, the slip function is spatially quite uniform. The static slip is given by $\Delta\sigma w/\rho\beta^2$, in agreement with estimates based on elastostatic solutions. The numerical simulations predict a rise time of $w/2\beta$ and peak slip velocity of $\sqrt{2fw/\beta}\ \Delta\sigma/\rho\beta$. In these expressions, w is the fault width, $\Delta\sigma$ the stress-drop, f the maximum frequency, β the shear speed, and ρ the density.

Careful studies of the broadband character of earthquake teleseismic signatures indicate that the relative excitation of long- and short-period waves is inconsistent with predictions from the simple model. In addition, a few isolated, severe stopping phases dominate near-field accelerograms synthesized from the simple model, in conflict with strong motion data. More complex rupture physics is required to explain the discrepancies between the model predictions and teleseismic and strong motion observations. In particular, a better physical description of the cessation of rupture growth appears necessary.

A displacement-weakening constitutive model, described by Figure 11, has been applied to simulate spontaneous rupture in the presence of both uniform and heterogeneous prestress.

21

YIELD STRESS σ_0

TECTONIC STRESS σ_T

FRICTIONAL STRESS σ_f

0   D_0

FAULT SLIP
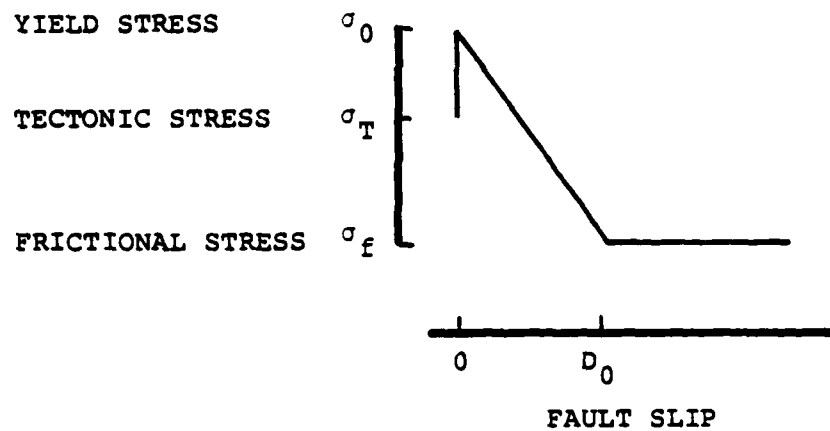
Figure 11.   Displacement-weakening constitutive model for the fault zone.

In this model of failure, the shear strength of the fault zone is assumed to be a decreasing function of its deformation; energy is dissipated during rupture extension and shear stress is bounded on the fault edges. When rupture initiates in a limited region of high stress (Figure 12a), the model leads to spontaneous propagation, deceleration and stopping of faulting. Figure 13 shows the evolution of the rupture front in this case, as well as the far-field P and S wave displacement spectra and the corresponding displacement, velocity, and acceleration pulses. In the presence of multiple high-stress regions (Figure 12b), each isolated stress concentration behaves roughly as an independent event. As shown in Figure 14, rupture velocity becomes quite irregular, and is strongly coupled to peak velocity of slip on the fault surface. Figure 15 shows the irregular rupture growth, as well as the far-field spectra and time-domain pulses which result. Predicted accelerograms are in better qualitative accord with strong motion data.

The model predicts significant consequences for the spectral and time-domain characteristics of the earthquake teleseismic signal due to the presence of stress irregularities. For example, Figure 16 compares the short-period teleseismic P-wave for the stress-concentration model with that for a uniform stress model (scaled to a source dimension equal to the dimension of the stress concentration). Both the period and amplitude of the b phase (first peak-to-trough) agree for the two models, while the stress-concentration model has twice the moment of the uniform stress model. The two events have been superimposed on an m_b versus M_s plot (from Filson and Bungum, 1972) to illustrate that the stress-concentration phenomenon enhances separation of earthquake and explosion populations.

23

(a) STRESS-CONCENTRATION MODEL
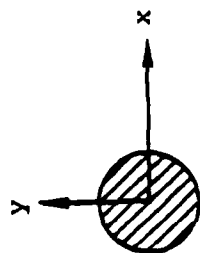
(b) MULTIPLE STRESS-CONCENTRATION MODEL
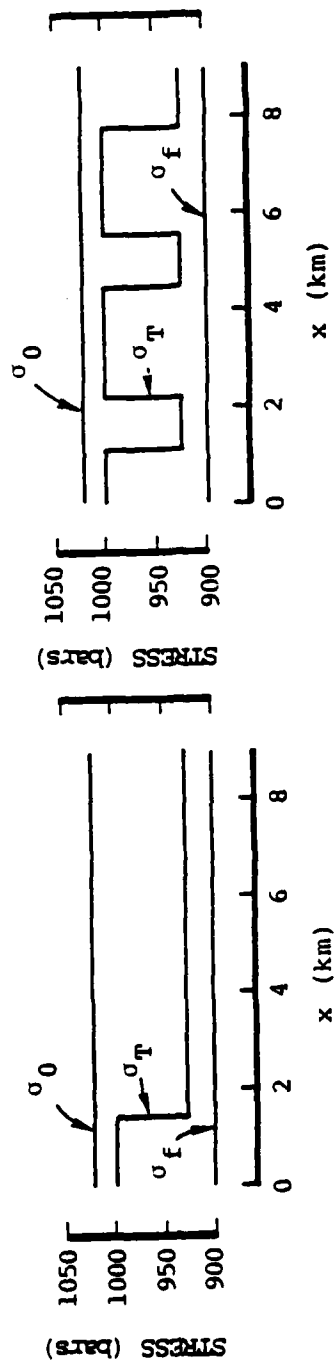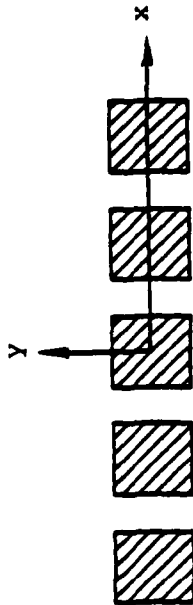
Figure 12. Stress-concentration fault models considered in this study.

24
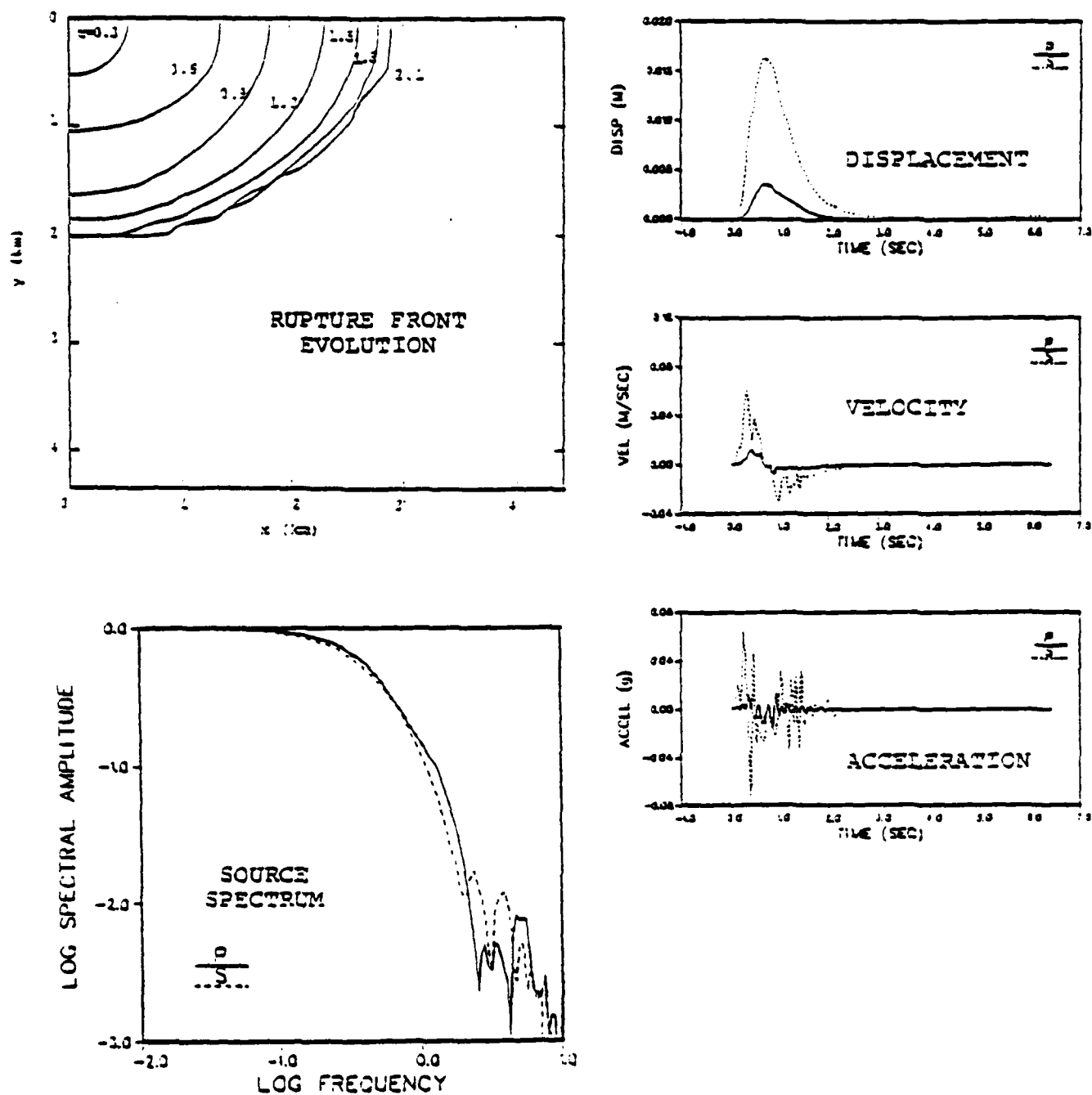
Figure 13. Rupture mechanism and far-field spectra and pulse
shapes for stress concentration earthquake model
at spherical coordinates θ = 45°, φ = 45°, rela-
tive to fault normal.

25
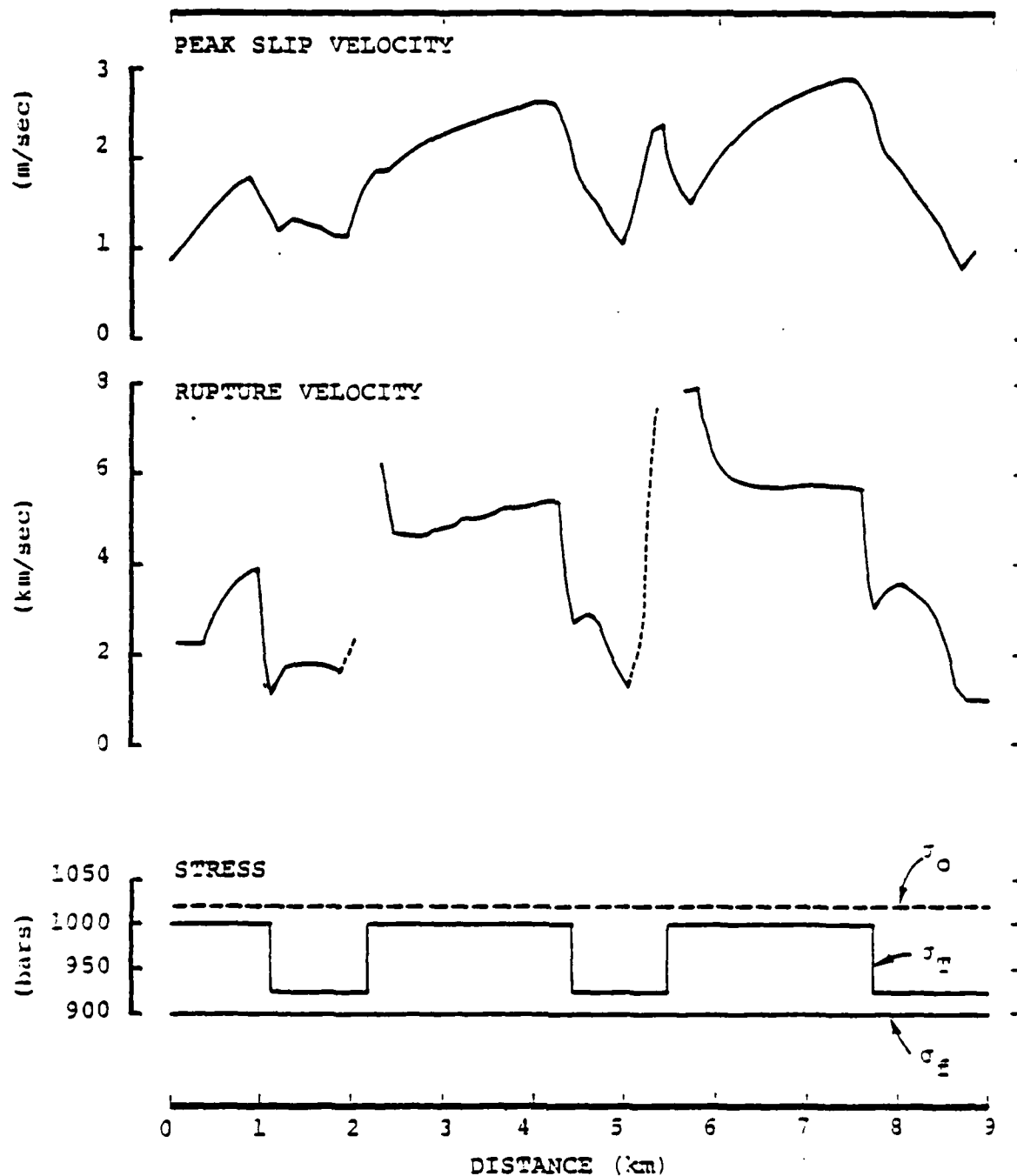
Figure 14. Peak slip velocity (low-passed, 5 Hz cutoff) and rupture velocity along the x axis, for multiple stress-concentration model. Dashed curves for rupture velocity indicate regions which ruptured out of sequence. For example, rupture occurred at x = 5.6 km while the region between 5.0 and 5.6 km was still intact.
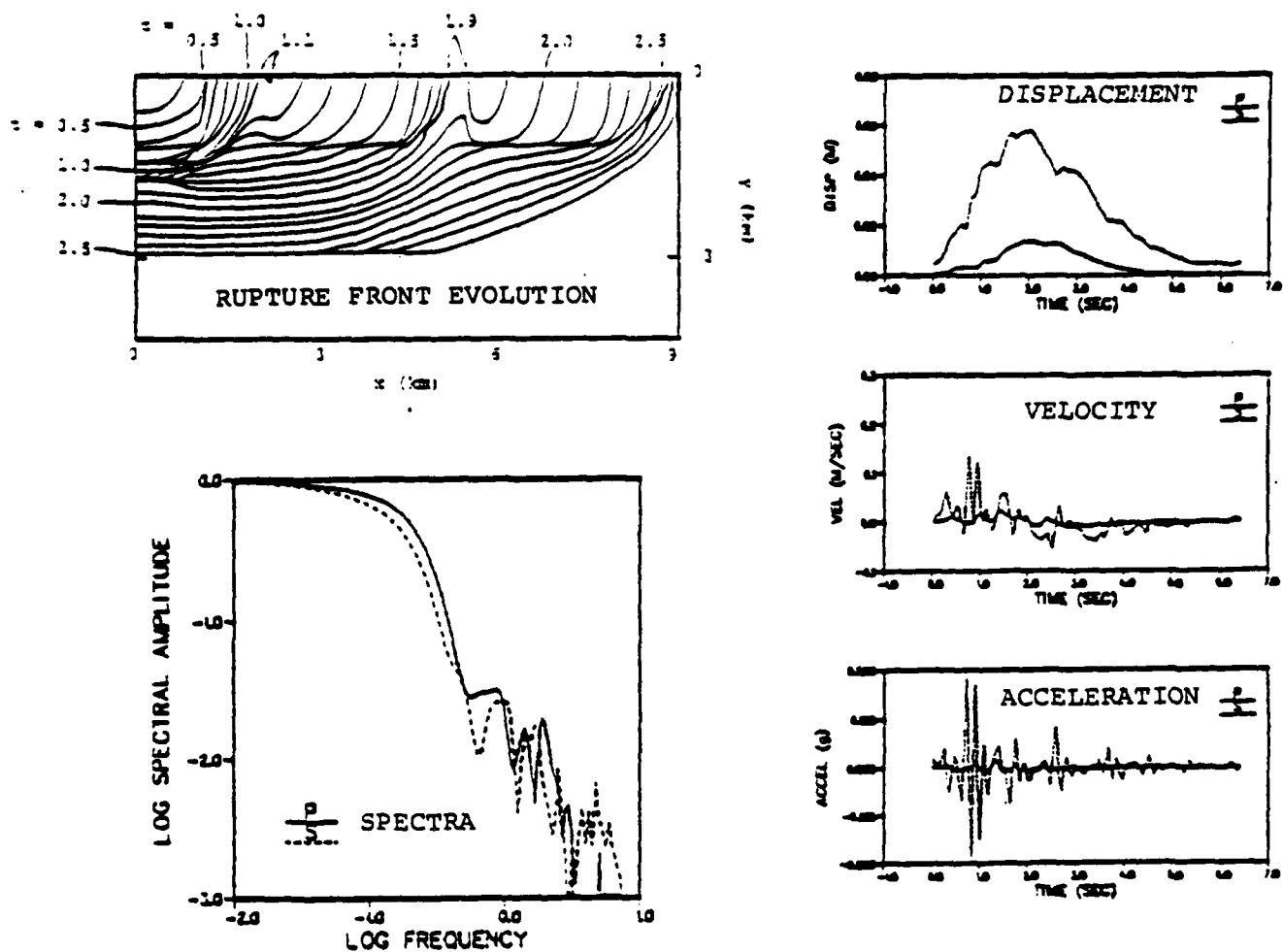
Figure 15. Rupture mechanism and far-field spectra and
pulse shapes for multiple stress-concentration
earthquake model (at spherical coordinates
θ = 45°, φ = 45° relative to fault normal).

27
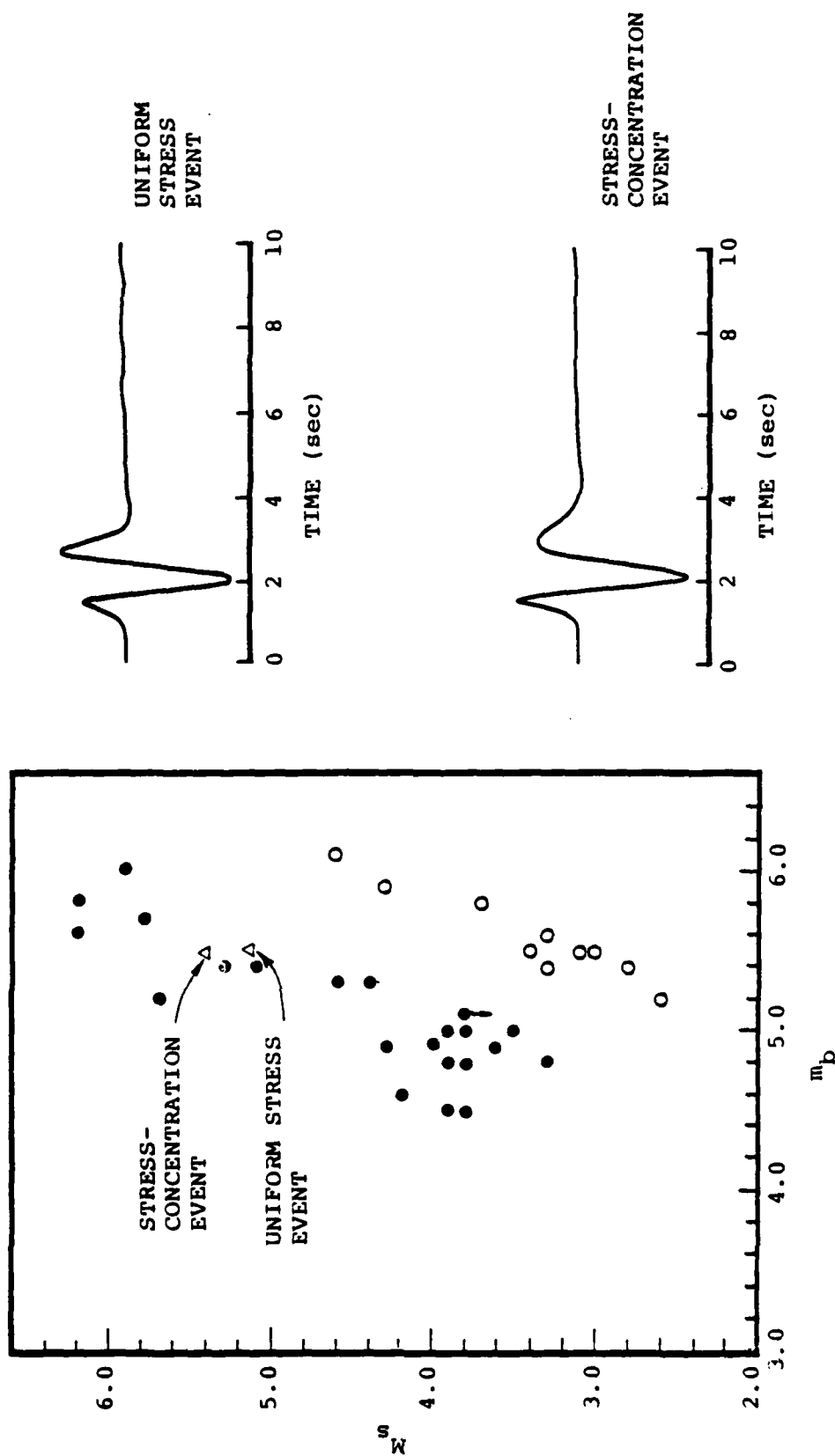
Figure 16. Short-period P-waves from uniform stress model and stress concentration model. The two events are plotted as triangles on an m_b-versus-M_s diagram (from Filson and Bungum), in which open circles and closed circles represent presumed explosions and earthquakes, respectively.

28

2.4 A SIMULATION STUDY OF THE DETECTABILITY OF A 5.3 KT DECOUPLED EXPLOSION AT REGIONAL DISTANCES IN THE EASTERN UNITED STATES BY J. R. MURPHY AND T. J. BENNETT

A detailed description of this research has been previously provided in the Semiannual Technical Report by Bache, et al. (1980a). For completeness, we include below an executive summary of objectives and accomplishments.

2.4.1 Objective

The objective of this task has been to conduct a preliminary theoretical evaluation of CTBT evasion capabilities associated with the cavity decoupling evasion scenario. In particular, the investigation has focused on extending the existing regional seismic data base for explosions in the eastern United States by theoretically scaling observed SALMON data to simulate the seismograms to be expected from a hypothetical, fully decoupled 5.3 KT explosion at the SALMON shotpoint.

2.4.2 Accomplishments

Four eastern United States stations were selected for analysis: Eutaw, Alabama (EUAL, Δ = 246 km), Cumberland Plateau Observatory, Tennessee (CPO, Δ = 623 km), Beckley, West Virginia (BLWV, Δ = 1065 km) and Wykoff, Minnesota (WFMN, Δ = 1437 km). The locations of these four stations are indicated by squares on Figure 17 which provides a map view of the North American Stations which recorded the SALMON event (Jordan, et al., 1966). The observed vertical component SALMON data recorded at these four stations have been theoretically scaled (Murphy, 1977) to the ground motion to be expected from a fully decoupled 5.3 KT explosion at the SALMON shotpoint. The selected theoretical decoupling factor (with respect to SALMON), corresponding to a simple step in pressure in a 39 m radius

29
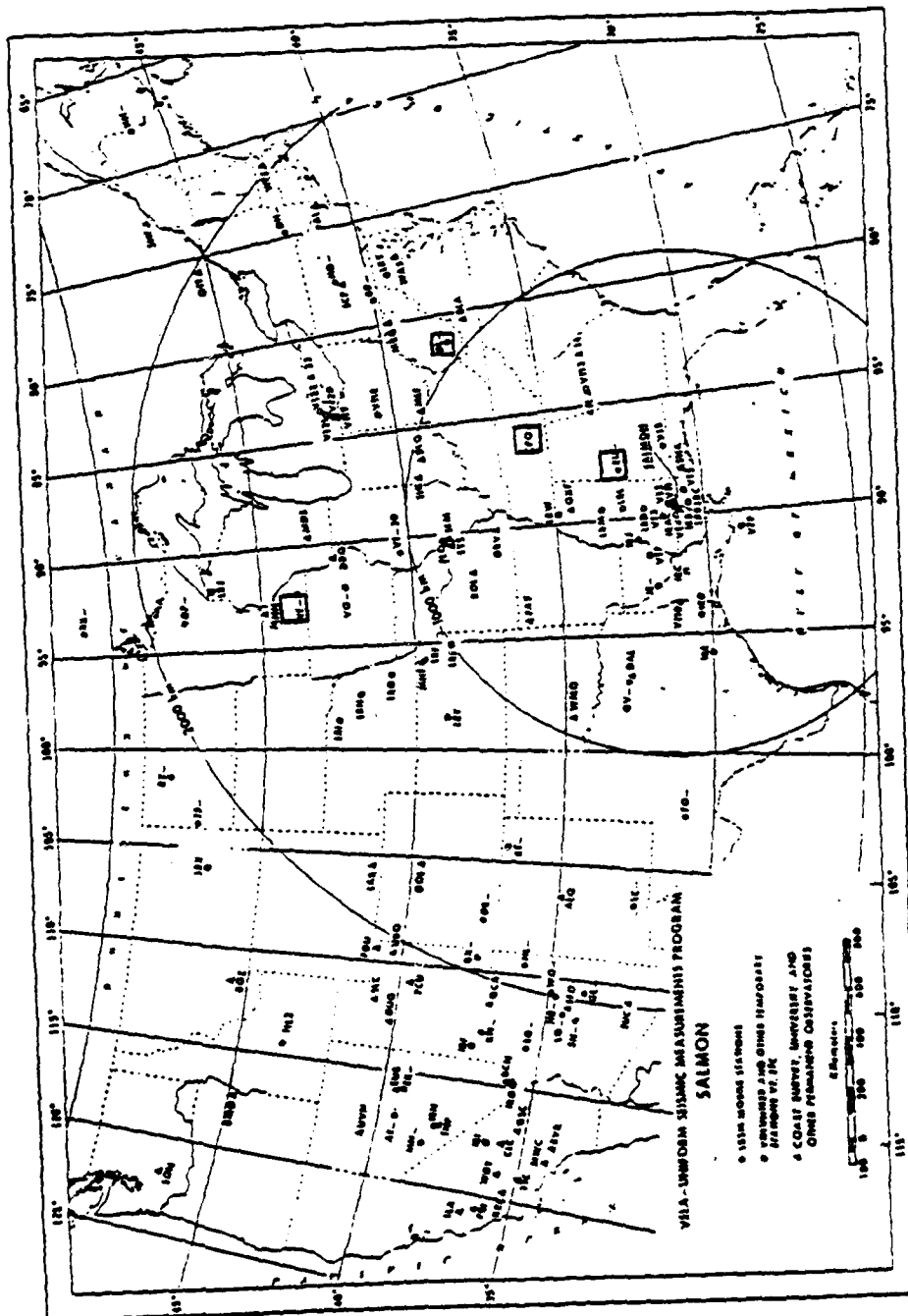
Figure 17. Map locations of regional SALMON stations (□) used in the decoupling simulation.

cavity, is shown in Figure 18. Observed SALMON vertical com-
ponent seismograms recorded at stations EUAL and WFMN are
shown at the top of Figures 19 and 20 respectively, where
they are compared with the corresponding simulated decoupled
seismograms (bottom). The simulated decoupled seismograms
were obtained by convolving the observed SALMON seismograms
with an operator defined by the ratio of the decoupled to
SALMON theoretical source functions. The traces shown to
the left of the simulated decoupled seismograms correspond
to samples of the noise recorded prior to SALMON at each
station, amplified so that they can be compared with the
estimated decoupled signal levels. This provides a basis
for assessing the detectability of the hypothesized decoupled
explosion at these stations under the local noise conditions
prevailing at the time of the SALMON experiment. A review of
this simulated data, as well as that from the other two
selected stations, indicates that, relative to the noise back-
ground prevailing during SALMON, a 5.3 decoupled explosion
would probably have been detectable on the short-period re-
cordings from the two nearer stations (EUAL and CPO) but not
from those expected at the more distant stations (BLWV and
WFMN). With respect to the lower noise background expected
at a modern, quiet site, the Lg phase from such a decoupled
explosion would probably be detectable at all four stations,
but initial P wave detection would still be questionable at
the two distant stations. Furthermore, as might be expected
on the basis of previous noise studies, increasing the effec-
tive bandwidth of the short-period data to encompass lower
frequencies does not improve this detectability due to the
fact that the noise level increases with decreasing frequency
while the decoupling factor remains essentially constant. By
the same argument, consideration of higher frequency data
should improve detectability, at least for high Q paths. How-
ever, it has not been possible to quantitatively evaluate

31
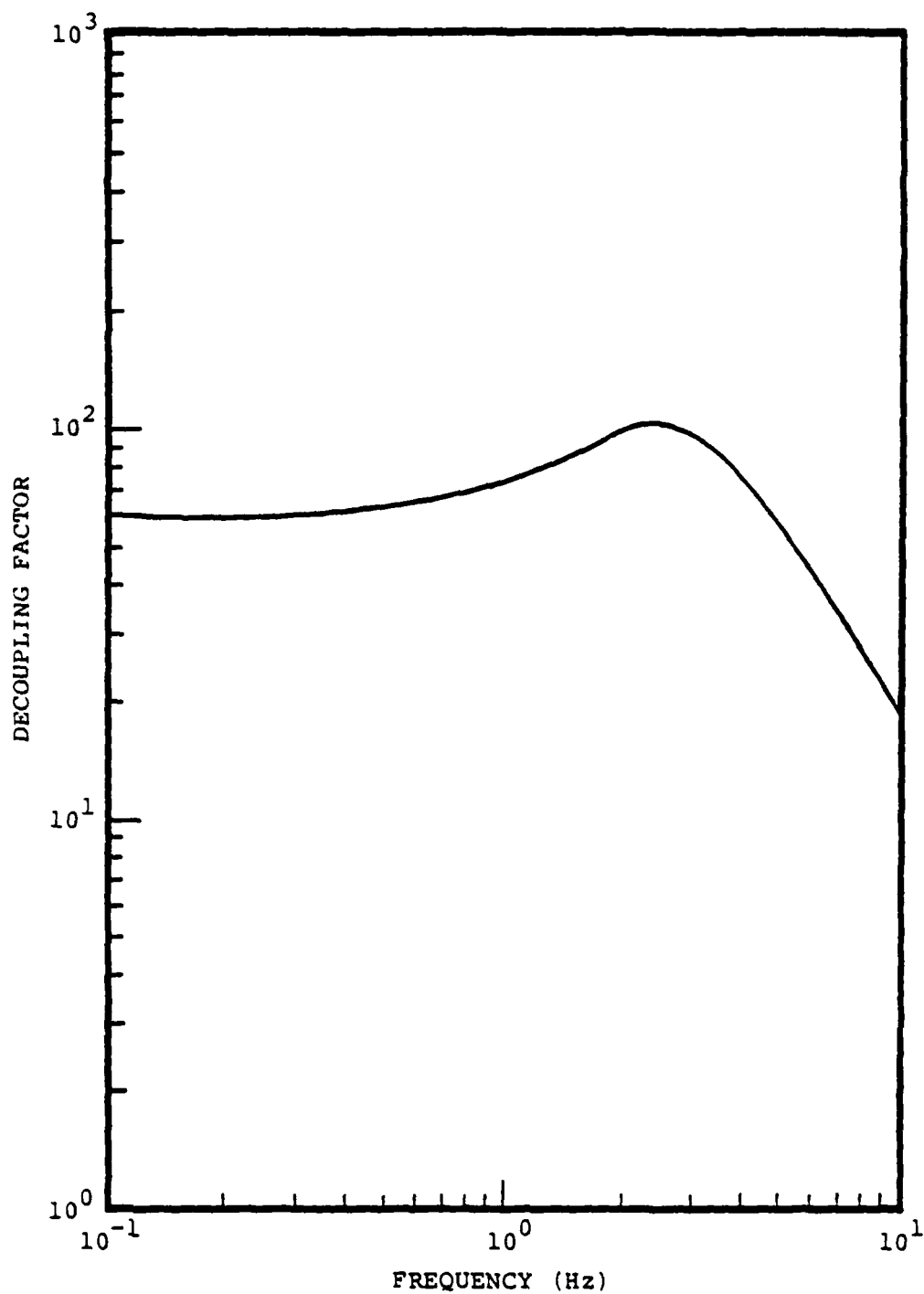
Figure 18.   Theoretical decoupling factor for 5.3 KT
             in a 39 m radius cavity in SALMON salt.

32
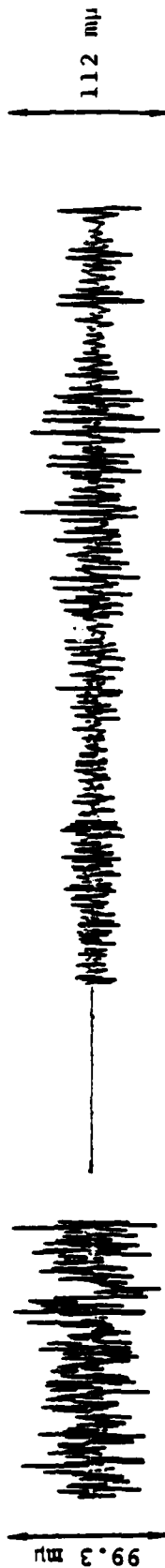
Figure 19. Comparison of observed SALMON and simulated decoupled vertical component seismograms, Station EUAL.

SALMON

8160 mμ

Decoupled 5.3 KT

112 mμ

20 Sec

SALMON Noise

99.3 mμ

33
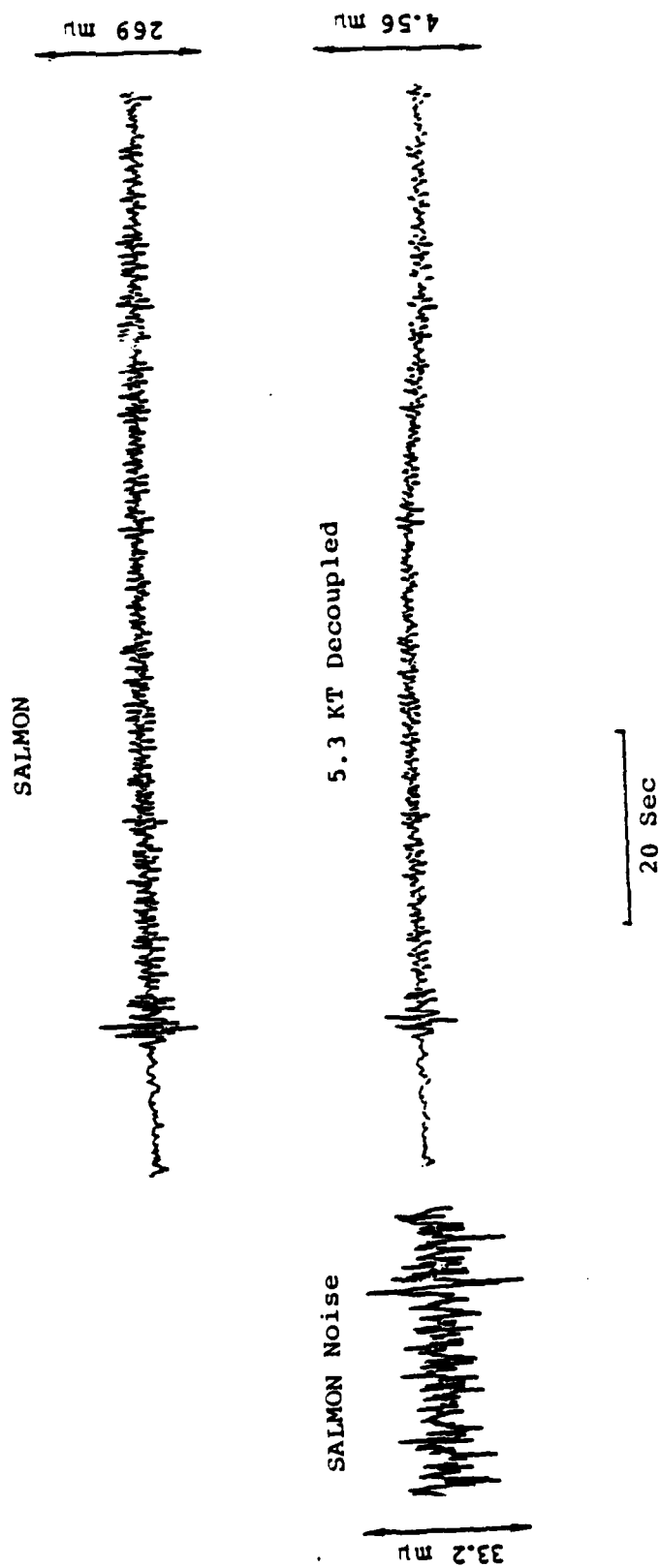
Figure 20. Comparison of observed SALMON and simulated decoupled vertical component seismograms, Station WFMN.

34

this potential improvement using the available data set due
to the relatively low sampling rate employed in the digitiza-
tion.

35

III.   REGIONAL SEISMOLOGY

3.1   INTRODUCTION

The work reported in this section pertains to Task 4.2.
It must be noted that several of the numerical calculations
performed under Task 4.1.1 for buried explosions have been
used extensively for the purposes of the present task and
have, therefore, not been described in Section 2.2 of this
report.

The results pertinent to the present section have been
the object of a detailed S^3 report by Bache, et al. (1980b).
They have also been summarized in the Semiannual Technical
Report by Bache, et al. (1980a). For this reason, we only
include for completeness an executive summary in the following
subsection.

3.2   CONTRIBUTION OF TWO-DIMENSIONAL SOURCE EFFECTS TO THE FAR-FIELD SEISMIC SIGNATURES OF UNDERGROUND NUCLEAR EXPLOSIONS BY T. C. BACHE, T. G. BARKER, N. RIMER AND J. T. CHERRY

3.2.1 Objective

As the contract evolved, the objective of Task 4.2 be-
came to study the far-field seismic waves from a series of
two-dimensional explosion calculations done under Task 4.1.1.
The purpose was to determine the importance of nonlinear
interaction with the free surface (including spallation) and
the depth-dependence of overburden pressure and material
properties. While the potential importance of these two-
dimensional effects has long been acknowledged, previous
attempts to model the seismic signatures of underground
explosions have almost all employed spherically symmetric
point source representations. A quantitative understanding

36

of the potential influence of higher order source effects is important for delineating the validity of this convenient approximation.

3.2.2 Accomplishments

The results summarized here are extracted from a 1980 S^3 report by Bache, Barker, Rimer and Cherry. The report presents a detailed analysis of the seismic waves from eleven two-dimensional finite difference calculations of underground nuclear explosions in granite. Seven were 150 KT explosions at depths from 159 to 1000 meters done by J. Trulio and N. Perl of Applied Theory, Inc. (ATI).

The other four calculations were done at S^3 with one intended to model the PILEDRIVER event. The constitutive model and source geology (three layers) were chosen for this particular event. As described by Rimer, et al. (1979), the computed and observed ground motions were compared at some twenty-five near-field gauge locations, where the agreement was quite good, except that the calculation overpredicted the amount of cracking (spallatic. This turns out to be important when comparing synthetic and observed far-field seismograms. The other three S^3 calculations were the same, except that the depth and yield were varied. The four calculations were as follows:

DEPTH (Meters)	YIELD (KT)
463	60 (PILEDRIVER)
1000	150
1000	20
400	20

The main results of the study may be summarized by plots of M_s and m_b versus source depth and yield. The observed values for the United States granite explosions PILEDRIVER, SHOAL and HARDHAT provide a standard for comparison.

In Figure 21, the M_s for all eleven calculations are plotted versus source depth. For this plot all M_s, including the observed value for PILEDRIVER, have been scaled to 150 KT by adding log (150/W).

In Figure 22, the M_s values are plotted versus yield. Also shown are the M_s from seismograms computed with reduced displacement potential (RDP) sources. The RDP calculations were done at S^3 for two depths (460 and 1000 meters) with the same constitutive models used for the two-dimensional calculations. Thus, comparing seismograms from the RDP and the two-dimensional calculations directly displays the influence of two-dimensional effects.

The m_b data from the ATI and S^3 source calculations are plotted versus source depth in Figure 23 and versus yield in Figures 24 and 25. Again, the values for comparable RDP sources are shown to directly display the two-dimensional effects predicted by the S^3 calculations.

The most important result of this study is that the S^3 calculations show M_s to be a strong function of depth. The shallow S^3 calculations have surface wave amplitudes that are a factor of two or three larger than those from a comparable one-dimensional source calculation. This effect is probably exaggerated because the free-surface interaction effects are too large in the S^3 calculations, but would remain important even with increased strength in the near-surface material. On the other hand, the ATI calculations show no strong dependence of M_s on depth, even though the shallow ATI sources cratered. We do not know why the two sets of calculations give such different results.

38
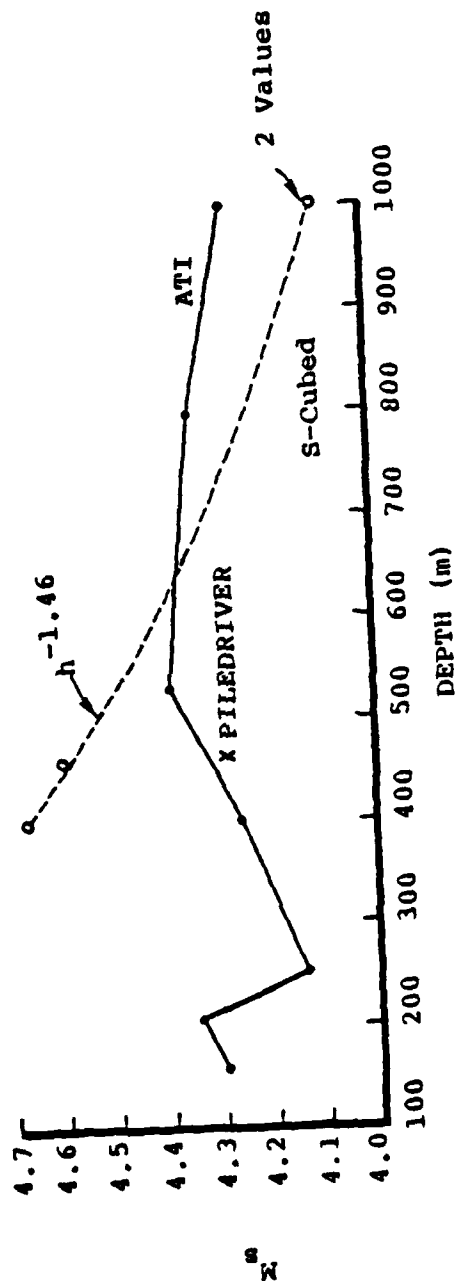
Figure 21. The M_s values for all the two-dimensional calculations are plotted versus source depth. The observed value for PILEDRIVER is also shown. All magnitudes have been scaled to 150 KT.

39

M_S VERSUS LOG YIELD
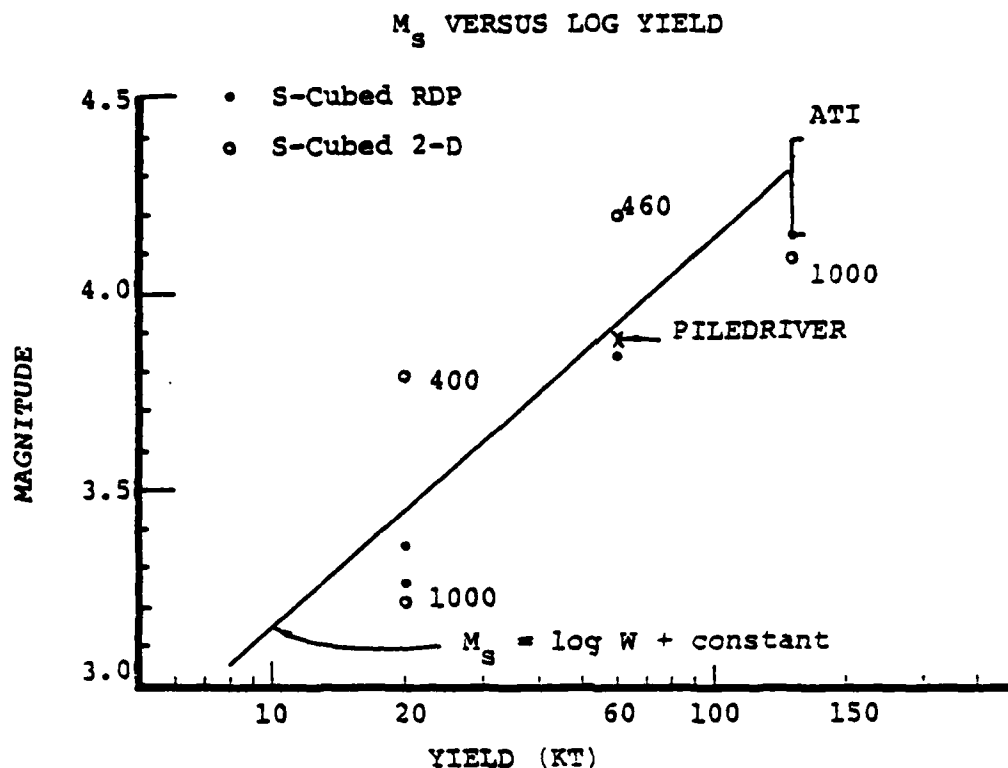
Figure 22. The M_S values for the S^3 RDP and two-dimensional source calculations are plotted versus explosion yield. The PILEDRIVER observed value and the range of M_S for the seven 150 KT ATI sources are also shown. The source depth of the S^3 two-dimensional calculations is noted with the M_S.

40
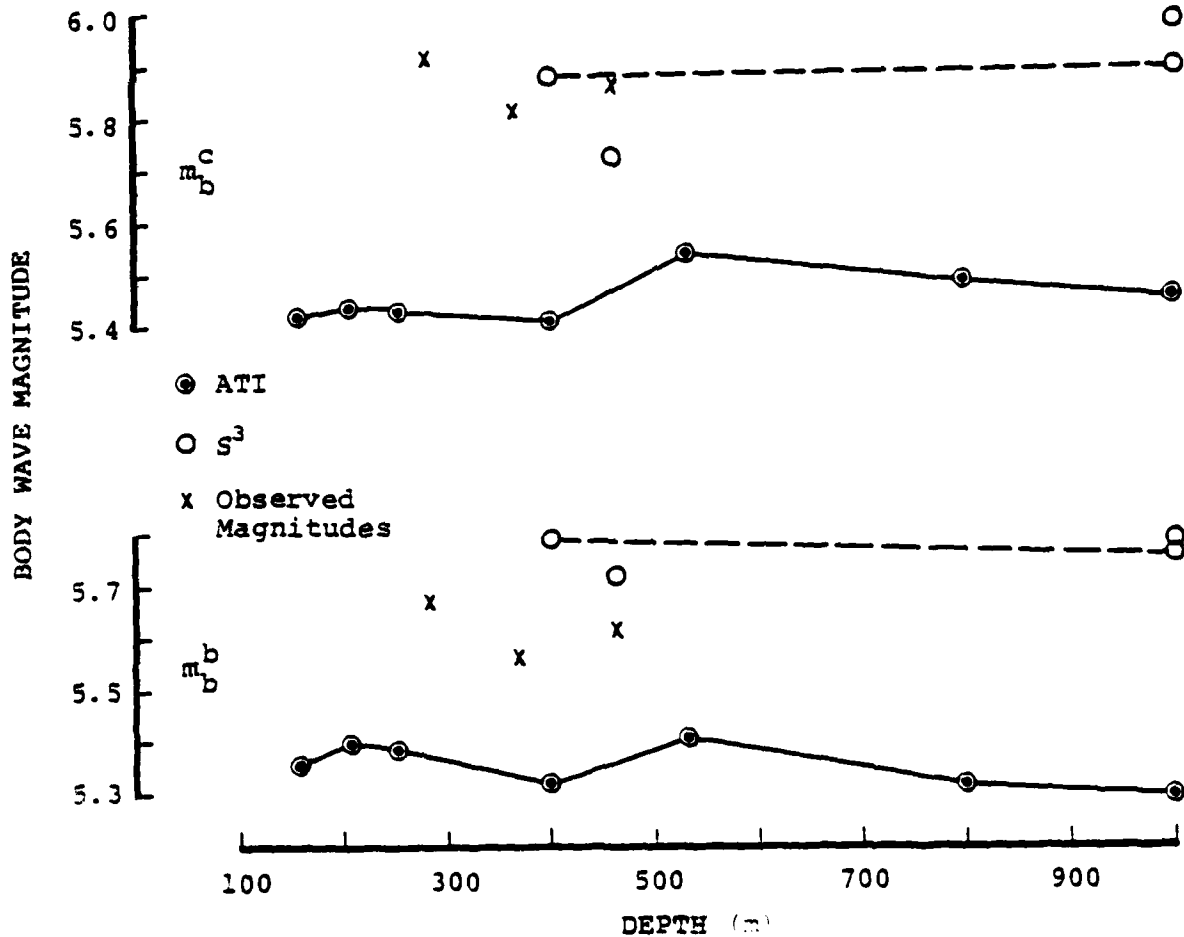
Figure 23. The m_b values for all the two-dimensional calculations are plotted versus source depth. The S^3 calculations at the same yield are connected with a dashed line. The observed values for HARDHAT, SHOAL and PILEDRIVER are also plotted with $m_b^b = m_b^c - 0.25$. All magnitudes have been scaled to 150 KT.

41

Figure 24. The b phase magnitude, m_b^b, is plotted versus yield. The values for the ATI calculations fall within the indicated range. The observed values are the published m_b^c minus 0.25 for HARDHAT, SHOAL and PILEDRIVER.

Figure 25. The c phase magnitude, m_b^c is plotted versus yield. Published (network average) magnitude values for HARDHAT, SHOAL and PILEDRIVER are also plotted.

43
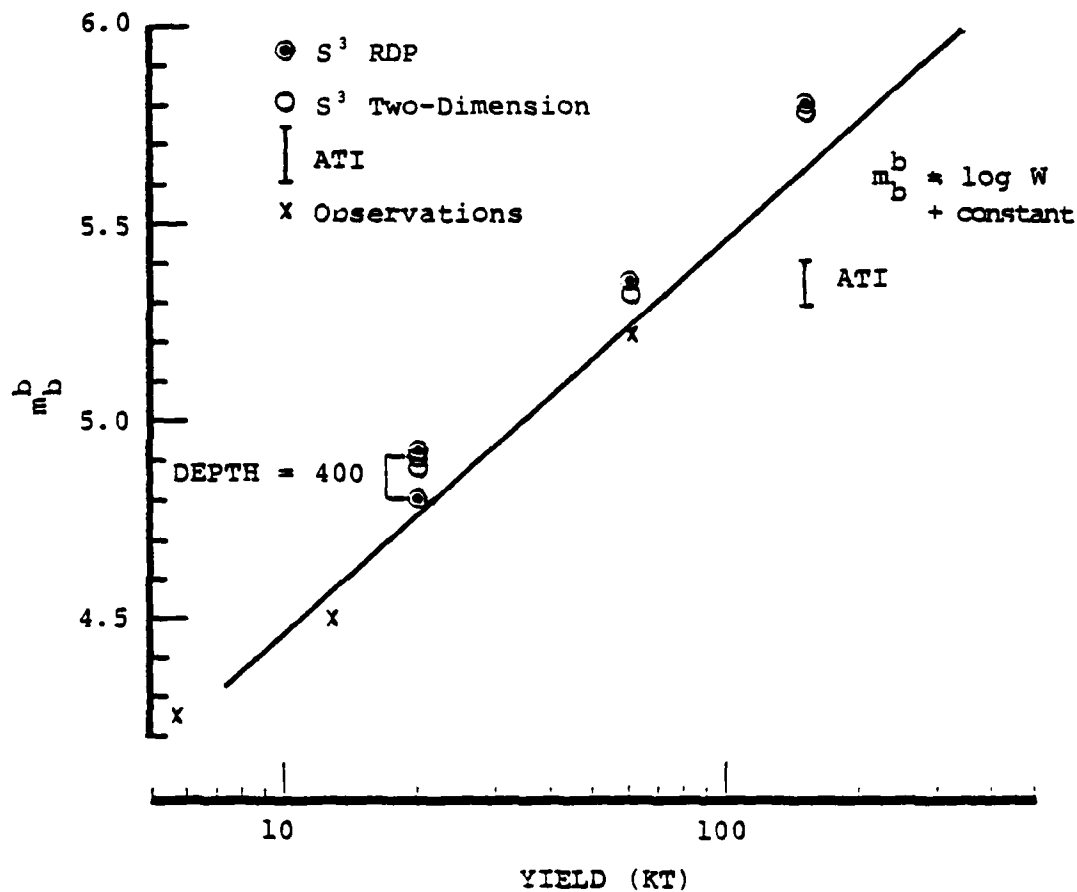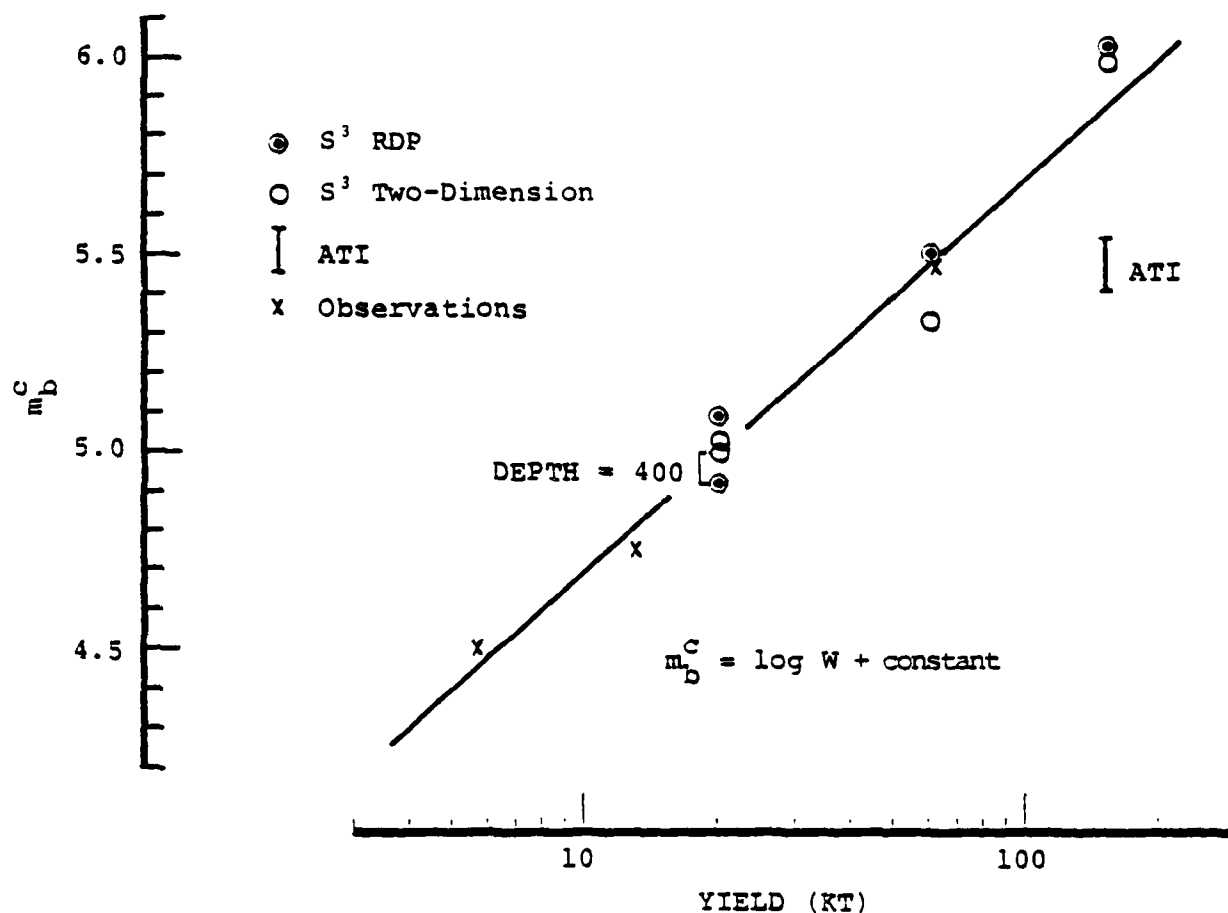
Comparison of waveforms, as well as the magnitude data in the plots, leads to the following conclusions:

Applied Theory, Inc. Calculations

- Neither m_b nor M_s are strongly dependent on depth. The most effect was on M_s at shallow depths.

- Compared to the semiempirical RDP source of Mueller and Murphy (1971), depth dependence in both amplitude and corner frequency is less for the ATI sources.

- The pP phase appears to be smaller than expected from elastic theory.

Systems, Science and Software Calculations

- Two-dimensional effects are not very important for the two deep explosions (20 KT and 150 KT at 100^ meters). Both m_b and M_s are little different from the values estimated from an RDP source computed with the same constitutive model at the same depth.* It is gratifying that these two very different and complex procedures arrive at the same results. This is true even though considerable cracking and spallation occur in the two-dimensional calculations.

- For body waves the first arriving P wave is essentially the same for one- and two-dimensional sources.*

- The two-dimensional effects enhance the surface wave amplitudes for the shallow events (60 KT at 463 meters and 20 KT at 400 meters) by a factor of two or three. We must quality this by pointing out that these shallow calculations have very strong surface interaction effects. Comparison with PILEDRIVER data indicates that the free surface interaction is

---

*These results are essentially tests of the entire computational procedure.

overpredicted, at least for that event. Less free surface interaction would presumably give less enhancement of the surface wave amplitudes.

- For the shallow events, the m_b^c is different than predicted with an RDP source, though by less than 1.2 units.

- Analysis of the spectra show that in no case is pP a spectral shadow of P, as it is for an RDP source and elastic propagation.

- Phases that seem to be associated with spall closure can be seen on the shallow source body wave records. However, they are not easily associated with identifiable crack closure patterns in the source calculation.

- Comparison of observed and calculated body and surface waves for PILEDRIVER leads to the conclusion that the two are in rather good agreement. This conclusion is subject to the qualifications one often faces in this kind of comparison. For the surface waves, it is the need to account for the *nonaxisymmetric* component, usually attributed to tectonic stress release. Adding a recent estimate for this component by Rivers and von Seggern (1979) to our solution, we get good agreement with the data. However, if the strike-slip solution of Toksoz and Kehrer (1972) is correct, the synthetic surface waves are about a factor of six too small.

- For body waves the comparison is complicated by the apparent presence of strong azimuthal effects in the radiated short period energy (Hadley and Hart, 1979). Our conclusion is that the computed PILEDRIVER source (in one- or two-dimensions) has about the right direct P amplitude. However, the two-dimensional source calculation appears to include too much nonlinear interaction with the free surface. The later portion of the P waveform does not match the data, apparently because pP is too greatly suppressed and because the seismic energy from spall closure is too large or is timed incorrectly. This "overprediction" of surface interaction effects is expected since comparison of theoretical and observed near-field motions and plots of the cracking near the source indicate that there was too much spallation in the calculation.

45

- The constitutive models used by S^3 (in spherically symmetric source calculations) lead to RDP source functions that are strongly peaked, with the value near 1 Hz a factor of five or more larger than the value at long periods. The peaking is due to the incorporation of an effective stress law and the choice of unconfined compressive strength (0.75 kb), based on laboratory data for fractured granite and results of comparison with near-field ground motion observations.

- While we do not have RDP source functions for the ATI granite, comparison of M_s and m_b for the ATI two-dimensional calculations indicates that the RDP peaking is probably less than a factor of two. Due primarily to this difference, the m_b for the S^3 calculations is about 0.5 units higher than that for ATI calculations of the same yield. The ATI M_s values fall between those for the shallow and deep S^3 calculations.

46

IV. AUTOMATIC SIGNAL PROCESSING

4.1   INTRODUCTION

This section reviews accomplishments during the contract period on:

> **Task 4.3.1** - Development of the MARS Detector,
>
> **Task 4.3.3** - Review of Seismic Event Detectors.

Although we had hoped initially to run the MARS (Multiple Arrival Recognition System) detector at VELA Seismological Center (VSC) in an on-line experiment (Task 4.3.2), it was not possible to perform this task. The principal reason for this was the decision to commit the resources allocated to Task 4.3.2 to the MARS detector task (4.3.1). The results which were obtained from this added effort were:

1. Increase in efficiency obtained by development of heterodyne technique.

2. Extensive analysis of signal-to-noise ratios using the modern theory of statistical signal analysis.

Results on Task 4.3.1 are described in the next subsection, where the MARS detection algorithm is described, together with an evaluation of its performance in an off-line mode on a suite of test tapes supplied by VSC, containing both noise and signal recordings. A more complete description may be found in Farrell, et al., 1980. Results on Task 4.3.3 have been detailed in a separate report to VSC (Berger, 1980) and we give below an executive summary of the most salient points and recommendations.

47

4.2 MARS SEISMIC DETECTION, BY W. E. FARRELL, R. C. GOFF AND J. WANG

4.2.1 Objective

The objective of this task was to optimize the MARS-based signal detection algorithm and evaluate it in an off-line mode on data supplied by VSC.

4.2.2 Accomplishments

The principal accomplishment has been the development of an efficient code which has been tested on four hour noise samples from NORSAR and Pinedale, and on the 24-hour NORSAR and Pinedale test tapes supplied by VSC. Results from both test tapes, which contained over 30 signals at each of four different amplitude levels, were comparable to the VSC bench-mark run; that is, at similar false alarm rates, about the same pattern of events was detected. On the UNIVAC 1100/81 the algorithm runs at 40 times real time on the 10 sample/second NORSAR data. As with the VSC detector, most of the time (80 percent) is consumed by Fourier transforms.

As an example of the current state of the MARS detector, Figure 26 shows the first ten NORSAR signals extracted from the 24-hour test tape. Each signal was buried in noise at four distinct amplitude levels, which Blandford refers to as "raw signal-to-noise ratio 1/2, 1/4, 1/8, 1/16." We refer to these four scaled copies as signal classes A, B, C and D. Thus, the plot shows ten A class events, those with raw SNR of 1/2. Furthermore, the seismograms shown in this figure are not the actual data present on the tape, but they have been high-pass filtered through a filter with a 1 Hz corner frequency. This is to attenuate the long period energy which contains mostly noise power and very little signal power. The events are much less obvious in the broadband data (see Figure 29). For

48
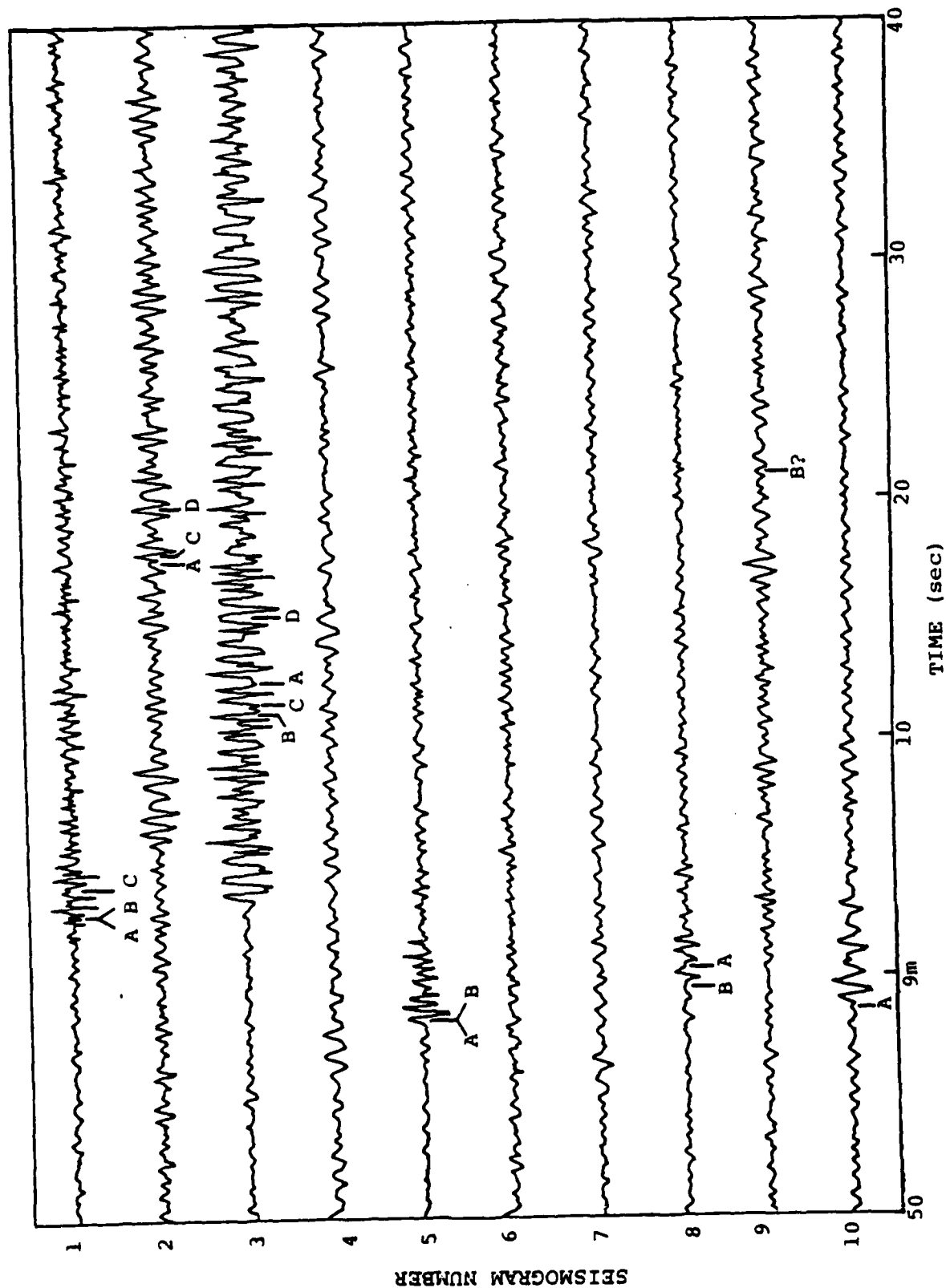
Figure 26. Events 1 to 10 from VSC 24-hour NORSAR test tape, high pass filtered. Letters A, B, C and D denote times of detection on signals with "raw signal-to-noise ratio 1/2, 1/4, 1/8, 1/16" respectively. There were 165 false alarms for this run over the 24-hour tape.

each seismogram we have shown the times at which "events" were detected by the MARS processor. Events labeled A were detections found in the A class seismograms, just the records shown here. Events labeled B were found on the B class seismograms, and so on.

The most important point to be made about these results is that the principal objective in the work to date has been to optimize the speed of the code and to calibrate the false alarm behavior. Thus, we have not "educated" it to look for specific signal types, nor to pick "first motion." Thus, the narrow band, long period motion in Event 2, is ignored in favor of later, broadband energy. Seismogram 3 is easily found at all four signal levels, but the peak in the broadband power falls well back in the Lg wave train.

It should be emphasized that no preprocessing or signal conditioning (e.g., optimum band-pass filtering) precedes the MARS analysis. Instead, the raw data is at the very first stage decomposed into a multiplicity of band pass channels. The signal amplitude in each channel changes dynamically as the background noise power rises and falls, as the shape of the noise spectrum changes with time, and as true seismic events come and go. By keeping a running history of noise amplitude in each channel, the MARS process then flags significant short term excursions, and finally searches for a pattern across the many frequency bands.

Among the subsidiary accomplishments in this automatic signal processing task, the most important are the following:

- A tenfold or more acceleration in processing speed was obtained by incorporating a heterodyne and decimate operation in the construction of the narrow band envelope function. Implementation of this feature was based on the observation that the spectrum of a narrow band

50

signal is band limited, and practically
vanishes outside a narrow region about the
center frequency. The heterodyne operation
is a signal processing device which shifts
the center frequency down to zero frequency.
But now the signal spectrum drops to a negli-
gible value at frequencies much less than
the Nyquist frequency. Then the inverse trans-
form back to the time domain can be accurately
found with a new and much smaller Nyquist fre-
quency.

● An extensive study was made of the statistical
properties of narrow band seismic noise. This
study was performed on the continuous envelope
functions, rather than the envelope maxima
catalog actually used by MARS, in order to be
able to relate the experimental results with
classical statistical theory. It was found,
for example, that the envelope probability
density function closely follows the Rayleigh
law, which is expected if narrow band envelopes
are extracted from Gaussian noise whose spectrum
is not too ragged. Further, the joint statis-
tics of multiple envelope functions were studied
to estimate the cross-correlation between two
envelope functions generated by different filters.
This work was necessary to quantify the possi-
bility of cross-correlation in envelope maxima,
and to give objective guidance both to the con-
struction of the comb of filters, and to the
significances of envelope alignments. Preliminary
work was undertaken in multiple envelope correla-
tion, using the Bernoulli trial model, but we have
not yet obtained definitive results.

51

- Working still with noise records, we know how to
  tune the MARS false alarm rate by adjusting the
  three key parameters: amplitude (normalized
  with respect to the noise in each band), band-
  width and dispersion. Figure 27 shows a cube
  in this parameter space, each cell of which
  contains a number related to the False Alarm
  Rate. The bigger this number, the poorer the
  detector. In our terminology, the bandwidth
  parameter is called k; it gives the number of
  envelope maxima (out of twenty possible) re-
  quired before an event is called. The amplitude
  parameter, also referred to as normalized ampli-
  tude cutoff in the third figure, expresses how
  large extrema must be before an envelope peak
  is to be included in the search for events.
  We refer to this as a normalized amplitude be-
  cause each envelope function in the time window
  currently being processed is scaled by the mean
  envelope amplitude of the previous N windows.
  There is, then, a floor on the minimum instan-
  taneous signal spectrum required before an
  event is called. The floor is just some multiple
  of the preceding noise spectrum. Finally, the
  dispersion parameter specifies how broad a time
  swath one permits the k peaks to fall within.

- Figure 28 shows a specific result selected from
  our noise study. It is a slice along the k = 6
  plane for a two-hour section of NORSAR data.
  The figure shows that the lower left hand corner
  is good, but that the upper right hand corner
  is bad. But we do not want to be too far down
  in the lower left hand corner. That gives great
  noise rejection, but concomitantly requires an
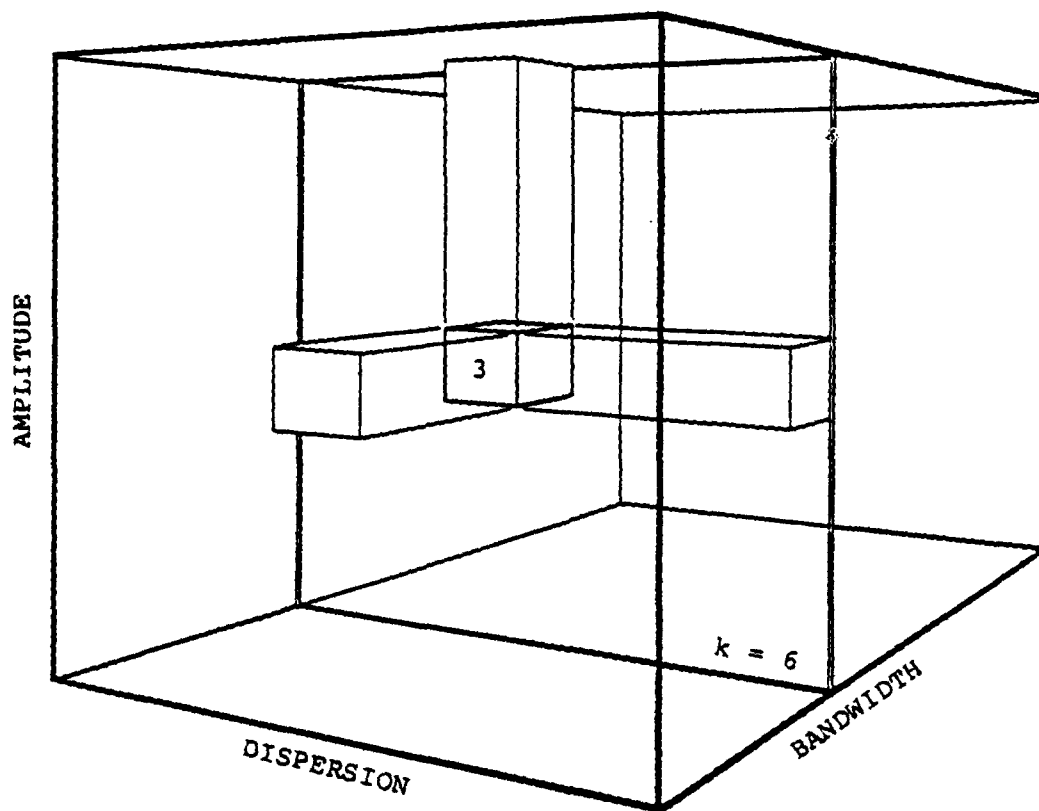
Figure 27. Schematic representation of the three-dimensional parameter space spanned by the key MARS detection parameters. Each cell within this cube contains a number giving the false alarm rate when the algorithm operates on pure noise.

53

HOW MARS DETECTION PARAMETERS AFFECT
FALSE ALARM RATES
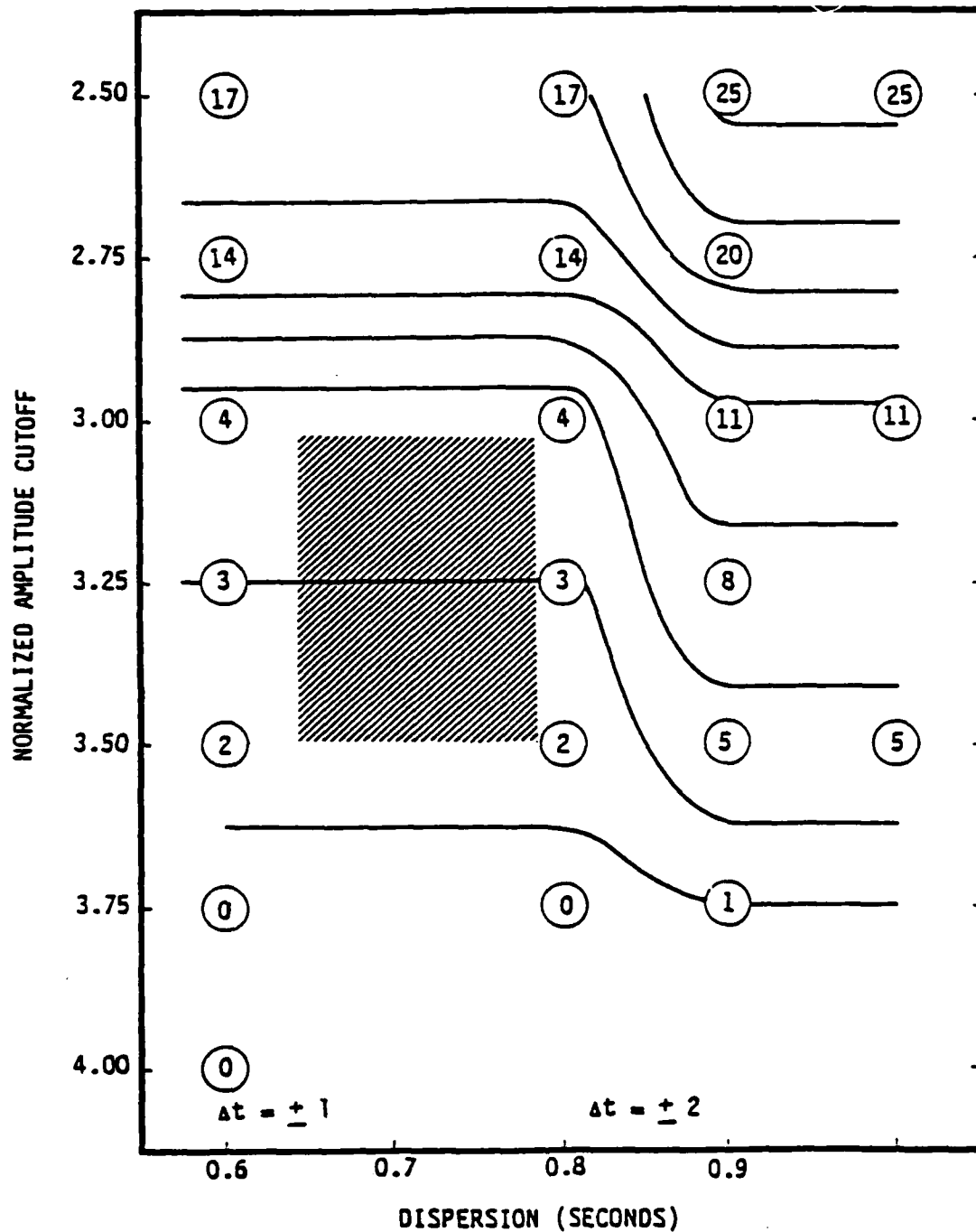
Figure 28. Contour plot giving number of false alarms in two hours of NORSAR data when k = 6 peaks are required to flag an event. Best region of operation is the hatched zone.

54

extremely large and impulsive arrival to trigger.
Thus, this part of the parameter space would show
a low probability of detection for easily seen
signals. To capture weak, moderately dispersed
signals, one wants to site the detector param-
eters somewhere in the hatched region.

- New graphical display procedures have been imple-
  mented for showing the time-frequency structure
  of seismograms. These have been found to be ex-
  tremely powerful tools in our research studies,
  and should be equally useful at seismic analyst
  stations for operational detection and discrimina-
  tion. Figure 29 displays the prebandpass filtered
  version of Seismogram 5 from Figure 26, along
  with its associated time-frequency decomposition.
  This is a true amplitude plot at each frequency,
  which clearly indicates the dominance of the
  long period noise, as does the comparison between
  this version of the seismogram and the bandpassed
  version in Figure 26. It can be seen, for ex-
  ample, that the best signal amplitude occurs
  over the 2.0 to 3.5 Hz frequency band. There
  is also significant signal power out to 5.0 Hz,
  but the noise there is so low, it is not possible
  to get an accurate estimate of the signal-to-
  noise ratio.

- Another type of display is shown in Figure 30.
  This display is similar to the sonogram display,
  long used in acoustic signal processing, but
  these figures were generated by digital rather
  than analog signal analysis methods. In this
  display, high power points in the time-frequency
  plane are shown as black zones, small amplitude
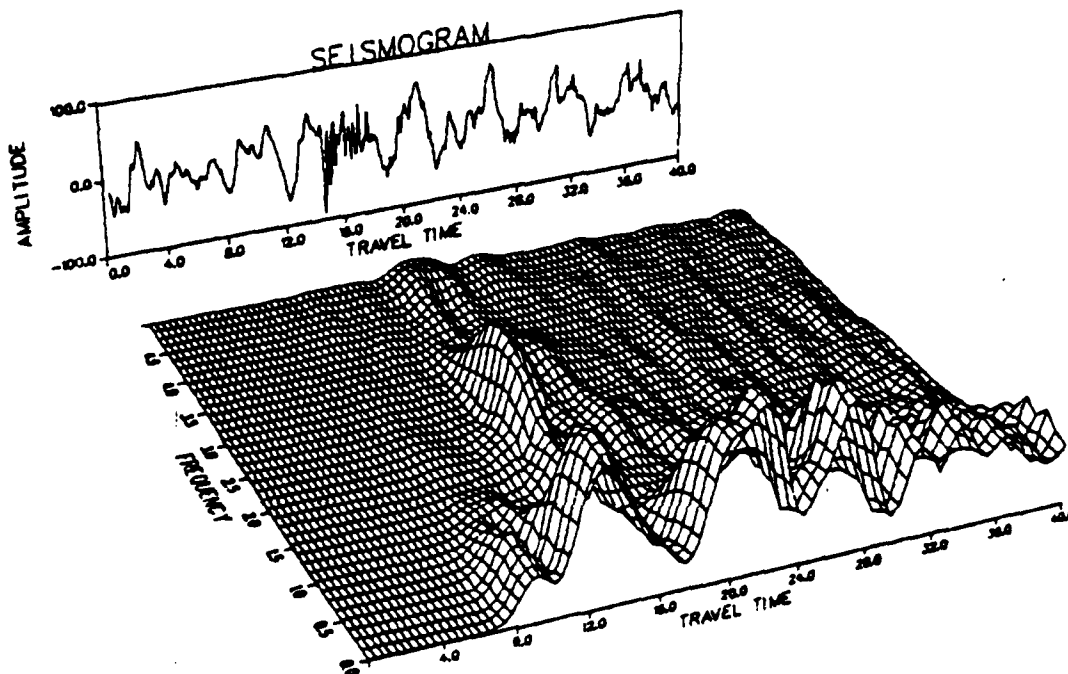
Figure 29.   Seismic Event 5 (see Figure 26) and its associated
             time-frequency decomposition. The fin at 16 sec
             (this time is arbitrary) and 2.5 Hz is the same
             event which appears at 56 seconds, 2.5 Hz in the
             middle panel of Figure 30. In this figure the true
             amplitude in each frequency band is preserved.
             This makes the predominance of the long period
             noise obvious. In Figure 30, the data has been
             "whitened" by scaling according to the largest
             amplitude in each band. This emphasizes frequency
             bands with good signal-to-noise ratio.
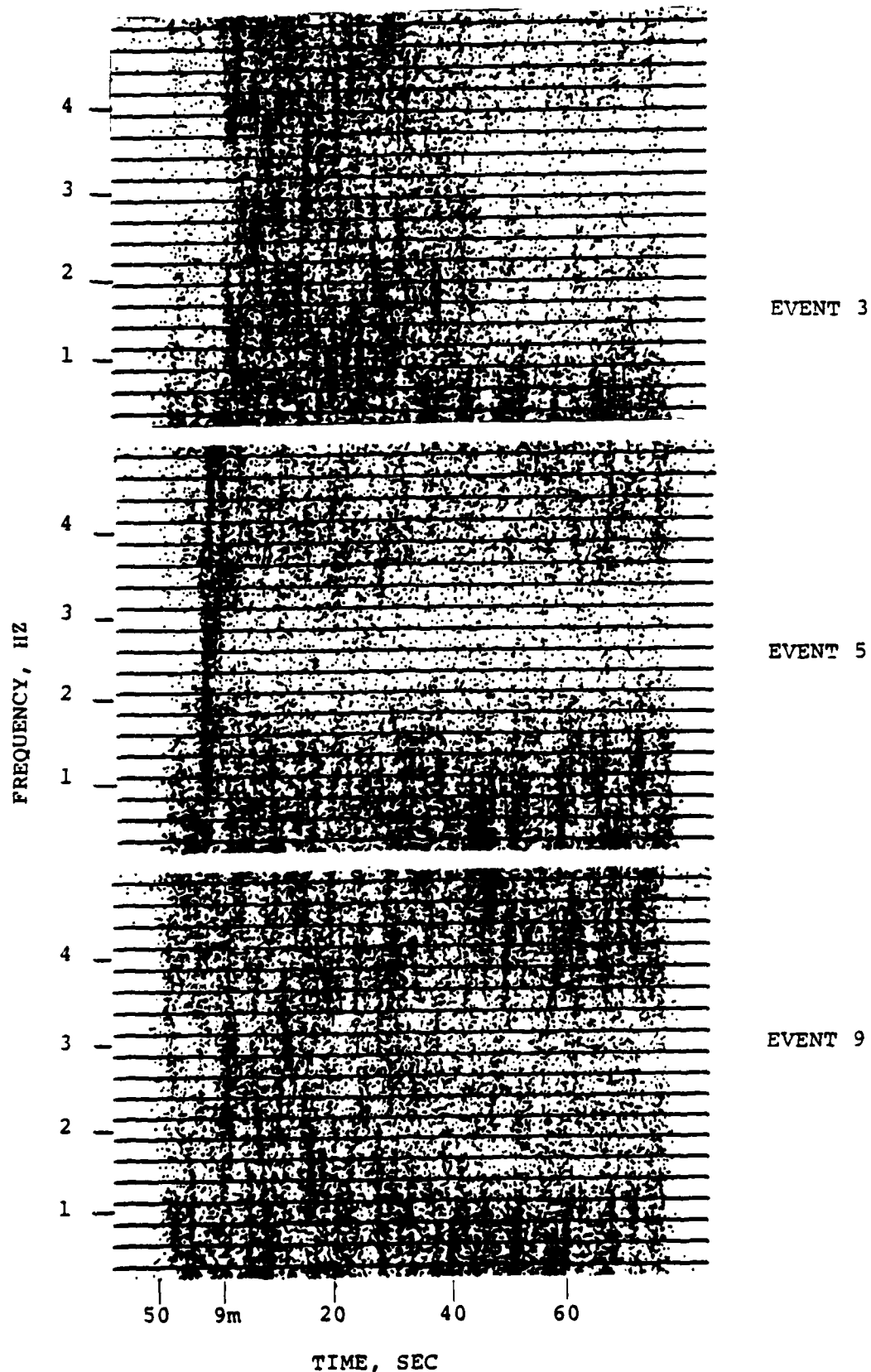
Figure 30.   "Sonograms" for seismic Events 3, 5 and 9 which
are also displayed in Figure 26.

57

regions shade down through various gray levels
towards pure white. Unlike the previous dis-
play, these data have been scaled according to
the "peak" power in each frequency band. This
tends to "whiten" any signals present, and make
more visible these frequency bands with good
signal-to-noise ratio.

- The extra frequency dimension in Figures 29 and
  30 tells much more about the nature of the
  seismic events than does the seismogram itself.
  Event 9, for example, is barely visible in
  Figure 26, but on Figure 30, it shows up as
  the dark band between 2.0 and 3.0 Hz, slightly
  later than nine minutes. One does see, of course,
  bands of similar length elsewhere in the figure,
  but they are not surrounded by the long gray zone,
  indicating they are most likely noise signals.

4.3 DETECTION STATE-OF-THE-ART BY J. BERGER

4.3.1 Objective

The objective of this review study was to identify
all pertinent automatic signal detection algorithms by equa-
tion, mathematical derivation and usage history, including
algorithms currently under development and scheduled to be
validated by October 1981.

4.3.2 Accomplishments

A draft report entitled "Seismic Detectors" The
State-of-the Art" has been prepared and submitted to VSC.
In this report, the following detection algorithms were
reviewed:

1. IBM

2. Z

3. Deflection

4. Analytic Envelope

5. Allen

6. Stewart

7. Walsh

8. MARS

General conclusions reached were:

1. All detectors reviewed in this report are based on a comparison between some form of variance estimate of the signal calculated over a time period approximately equal to the duration of an expected seismic event, and the normal (or long term) variance.

Possible exceptions to this general form are the phase detector described by Unger (1978) and the similar part of MARS. The former did not work because the short period phase fluctuations were so rapid that they could not reliably be predicted; the latter has not been implemented.

2. Ad hoc detection algorithms such as Allen's and Stewart's (1977) offer a hope of some improvement in the detection process. These methods, after having made the basic detection statistic test and having made a tentative identification, are followed by a further process that is designed to:

   a. reduce the false alarm rate,
   b. improve the timing capability, and
   c. speed the recovery of the detection
       algorithm after an event is encountered.

59

How much these algorithms can be expected to offer
significant improvements depends upon the noise environment
in which they are operating. If the SNR is such that a high
probability of detection is achieved with a tolerable FAR,
then little improvement can be expected. If, however, the
SNR is poor, so that the probability of detection is low for
a given FAR, then significant improvement may be achieved by
such two-stage algorithms.

3. Testing of the detectors described in this report
was not carried out in a uniform manner on the same or even
similar data sets. Thus, no definitive statement about their
relative performance may be made. However, it appears that
no one detector is obviously superior to all others. Some
have been optimized for teleseismic detection using a moder-
ately large computing facility. Some have been designed for
operation in microprocessor controlled field recording units,
typically used in the near field or at least at regional
distances. These applications stress ease of implementation
in microprocessors. Some algorithms stress timing ability as
this may be another object of the algorithm.

4. Little *theoretical advance has been achieved* since
Frieberger's 1963 work in which he "solved" the problem for
detection of a Gaussian signal in Gaussian noise. The influ-
ence of this work has rightly guided the design and implementa-
tion of many of the detectors used today. However, it must
not be thought that the "real problem" has been solved. The
"real problem" is the detection of certain nonGaussian signals
in the presence of nonGaussian noise. Frieberger discovered
the optimum detector for an approximate model of the actual
situation, but, other algorithms may work significantly better
on "real" data. Further, considerations such as timing ability,
recovery of the algorithm after an event, and immunity to
highly nonGaussian noise such as line spikes and data dropouts
may dictate very different approaches.

60

As a result of the review, the following recommendations were made:

- Uniform testing of all viable detectors should be conducted with

  a. a realistic synthetic data set;

  b. all detectors coded for and running on the same or similar machines;

  c. ROC curves produced for each detector comparing them with the theoretical performance of the detector for a completely known signal.

- Theoretical and experimental research in phase sensitive detectors should be supported as this is an area where it may be possible to exploit signal information not used in energy or power detectors.

- Research should be encouraged to test if matched filters for specific types of signals (station/source pairs) improves detector performance.

- Further development of hybrid detection algorithms, that combine high probability of detection with a high FAR and then are followed by a post processing to reduce the FAR should be undertaken.

- New algorithms, designed specifically for use with the new generation of three component broad band seismographs, should be developed and tested.

- In view of data rates from these new data sources, dedicated microprocessors to run the detection algorithms on a one processor per channel (or seismic station) basis should be considered.

61

V. EVALUATION OF SUITES OF EVENTS

5.1 INTRODUCTION

The objective of this task (Task 4.4 of our Contract F08606-79-C-0008) was to study and evaluate the feasibility of automatic determination of body wave magnitude using the MARS processor described in Section 4.2. In addition, the work included developing and testing of an analogous automatic surface wave magnitude algorithm.

This work is summarized in an S^3 Semiannual Technical Report (Bache, et al., 1980a). The next subsection summarizes the most salient results.

5.2 AUTOMATED MAGNITUDE $\hat{m}_b$ AND $\hat{M}_s$, BY T. C. BACHE AND B. SHKOLLER

In FY '79, we proposed an automated magnitude measure called $\hat{m}_b$ and tested it by processing high signal/noise recordings of eleven Pahute Mesa explosions at six teleseismic stations (Bache, 1979; Bache, Day and Savino, 1979). We concluded that the $\hat{m}_b$ was at least as good a magnitude measure and yield indicator as the most carefully determined time domain m_b. The $\hat{m}_b$ algorithm used in that earlier work did not account for the presence of seismic noise, and so was viewed as primarily a demonstration of the concept.

As part of the VSC conducted discrimination experiment, algorithms were constructed to compute variable frequency magnitudes, $\bar{m}_b(f)$, at selected frequencies (Masso, et al., 1979; Savino, et al., 1980). These algorithms do incorporate corrections for the presence of interfering phases and seismic noise. Otherwise the $\hat{m}_b$ used by Bache (1979) is not much different from $\bar{m}_b$ (1 Hz).

In the current contract, we have implemented a new algorithm for $\hat{m}_b$ (which is essentially $\bar{m}_b$ (1 Hz)) and tested it by application to a series of synthetic seismograms which are constructed by embedding a signal of known $\hat{m}_b$ in seismic noise. The $\hat{m}_b$ has also been computed for a set of RKON recordings of Eurasian events taken from the AI data set. A similar algorithm has been implemented for computing an analogous $\hat{M}_s$, and some testing has been done.

5.2.1 Description of the $\hat{m}_b$ Algorithm

The calculation of $\hat{m}_b$ includes the following steps:

1. The seismogram is processed by MARS, which applies a suite of narrow band filters and constructs a table of envelope function peak amplitudes (A_c) and group arrival times (t_g).

2. The MARS detection algorithm is applied to identify an undispersed P wave arrival. This algorithm works with a "surface" like that is shown in Figure 31, where the A_c are plotted versus t_g and filter center frequency, f_c. For each f_c the largest A_c is denoted by an asterisk. The relative amplitudes of the other peaks are denoted by integers, with the asterisk given the value 10. The detection algorithm searches for a "ridge" of amplitudes with nearly the same t_g to find the group arrival time, $\bar{t}_g$, of a detected P wave. The "+" and "-" symbols in the plot denote a statistically determined uncertainty window within which any A_c could be associated with the detected signal.

3. For each f_c, one A_c is chosen to define the "MARS signal spectrum." This is done by a scoring algorithm which, in its current form, works fairly well, but could probably be improved for low S/N events.
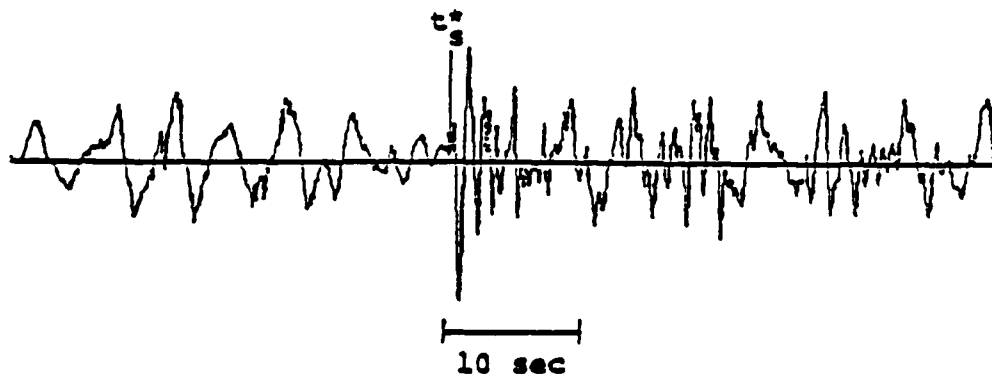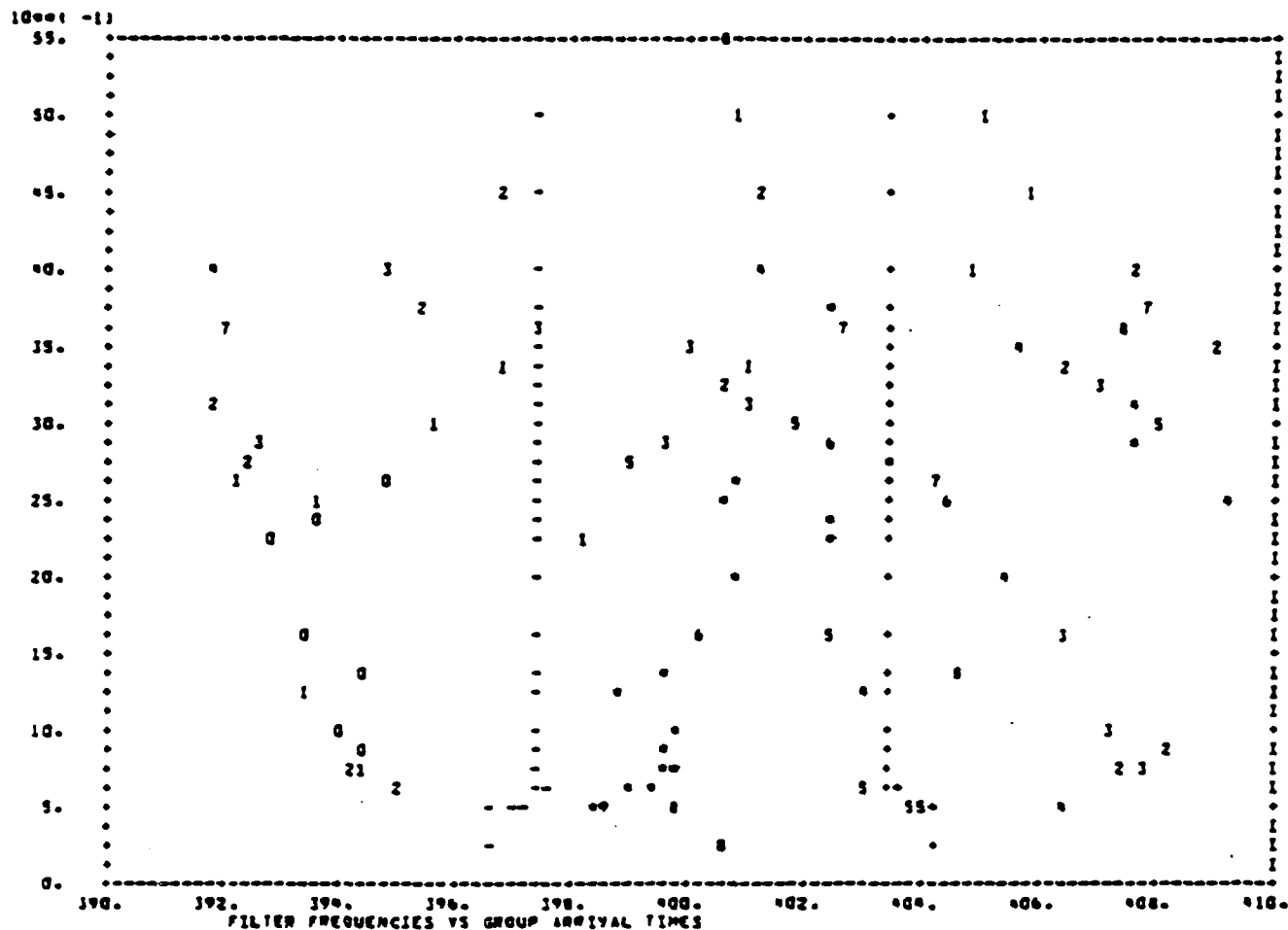
63

Figure 31. Bottom portion is a seismogram recorded at a station
in Bluff, Alaska, from an event in the Kurils. The
top half is a plot of filter center frequency versus
group arrival time (sec). The t_s^* with arrow attached
shows where the automated detection and first arrival
algorithms picked the signal arrival time.

4. The A_c values about a specific f_c (e.g., 1 Hz) are fit to give a "smoothed" estiment for the spectral amplitude at that frequency. This amplitude is corrected for the presence of nearby envelope peaks and a statistical estimate of the uncertainty is made, based on the "MARS spectrum" of the ambient noise. The $\hat{m}_b$ is computed from $\log (A_g^{**}; f_c) + B$, where A_g^{**} is the noise corrected A_c and B is the usual distance correction.

5.2.2 $\hat{m}_b$ Algorithm Testing

In Figure 32, we show the $\hat{m}_b$ for a synthetic seismogram which has been added to a noise sample from RKON, with the ratio of peak time domain amplitudes ("Peak S/N") being scaled to 100. The $\hat{m}_b$ is 3.589, which may be compared to the time domain $\hat{m}_b$ of 3.78, computed from $\log(A/T) + B$, with $T = 0.7$ seconds. Systematic differences between m_b and $\hat{m}_b$ are expected.

The same synthetic was added to various segments of noise recorded at RKON. Some examples are shown in Figure 33. Bache, et al. (1980) show fifteen such examples. The error in arrival time and $\hat{m}_b$ for these examples are tabulated in Table 1. Only when the ratio of MARS signal spectrum to MARS noise spectrum gets to be 1.5 or smaller are the errors very large. That is, even when the signals can barely be detected by eye, the $\hat{m}_b$ algorithm is able to give a good estimate for the magnitude.

5.2.3 $\hat{m}_b$ for Actual Data

Bache, et al. (1980) present the $\hat{m}_b$ results for Eurasian explosions and earthquakes recorded at RKON and LASA. The epicentral distances are from 53 to 94 degrees and the events have PDE magnitudes from 4.8 to 6.0. The $\hat{m}_b$ algorithm appears to
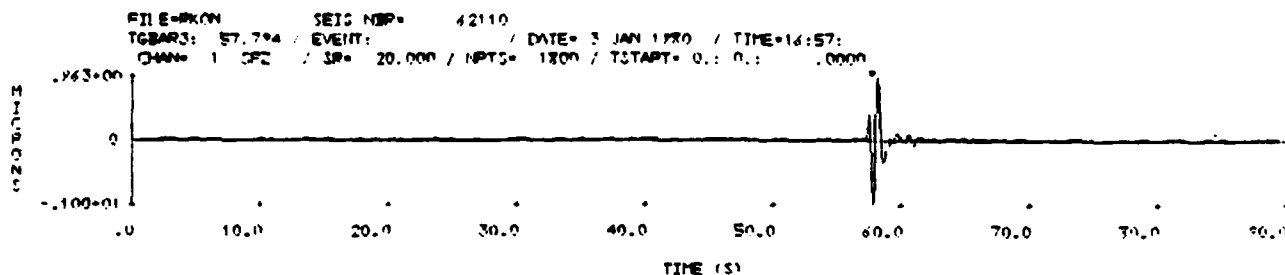
FILTER CENTER FREQUENCY (Hz)
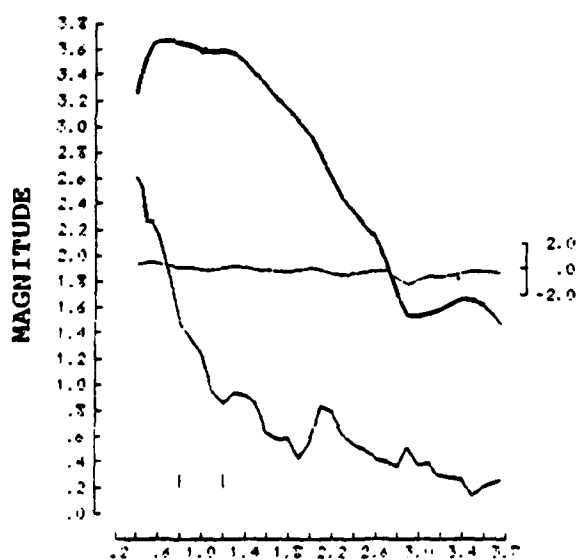
Figure 32. Calculation of $\hat{m}_b$ for a seismogram with peak synthetic/peak noise = 100. The seismogram is shown at the top with an asterisk denoting the signal arrival time t_g. The $\hat{m}_b$ calculation is shown graphically, with the heaviest line being log $(A_g^*; f_c)$ + B. The line of medium shade is the analogous magnitude for the noise. The light line is the t_g for each $A_g^*(f_c)$, with zero on the t_g scale (at right) being t_g. The $\hat{m}_b$ is computed at 1 Hz and is marked with an X. Printed above the graph are $\hat{m}_b$ (MB), the uncertainty in $\hat{m}_b$ imposed by the noise (± DMB), the noise magnitude at 1 Hz (MBNF), the mean signal/noise power over the frequency band from FLEFT to FRIGHT, and the B correction for the magnitude (BDEL).

66

Figure 33. Test of the $\hat{m}_b$ algorithm with noise Section 62110. The ratio of the peak amplitude of the synthetic to the peak noise amplitude is denoted by Peak S/N. The actual arrival time of the signal is the time of the asterisk plus t_A.

Figure 33. (continued)
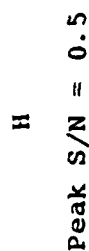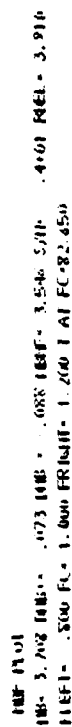
TABLE 1

SUMMARY OF $\hat{m}_b$ TEST CALCULATIONS

Identifier	Peak Signal / Peak Noise	S/N (1 Hz)	$\hat{m}_b$	$\hat{m}_b$ Uncertainty	$\hat{m}_b$ Error	Arrival Time Error
		Noise Section 62110				
(Figure 32)	100	217	3.589	0.001	–	–
A	3	6.5	3.583	0.018	-0.006	+0.02
B	1	2.2	3.593	0.055	0.004	0.03
C	1	2.6	3.667	0.046	0.078	-0.09
D	1	2.2	3.586	0.056	-0.003	0.48
E	1	2.2	3.581	0.057	-0.008	-0.01
F	0.5	1.5	3.734	0.082	0.145	0.09
G	0.5	1.2	3.622	0.110	0.033	-0.76
H	0.5	1.5	3.708	0.088	0.119	0.14
I	0.5	1.4	3.689	Missed Signal		
		Noise Section 274110				
J	100	219	3.586	0.001	–	–
K	1	2.0	3.546	0.111	-0.05	-0.05
L	1	2.2	3.595	0.095	0.09	-0.15
M	0.5	1.1	3.583	0.226	-0.03	-0.05
N	0.5	1.0	3.548	Missed Signal		

give excellent results, even when the signal is difficult to detect by eye so that time domain m_b measurements would probably not be attempted.

5.2.4 Description of the $\hat{M}_s$ Algorithm

The M_s algorithm is nearly the same as the m_b algorithm, except that the dispersion character of the surface wave signal of interest must be specified explicitly. The $t_g - f_c$ plane (Figure 31) is first mapped into a $t_g' - f_c$ plane where a signal with the expected dispersion appears to be nearly undispersed. The algorithm then follows the same steps as for $\hat{m}_b$.

5.2.5 $\hat{M}_s$ Algorithm Testing

In Figure 34, we show an example of the $\hat{M}_s$ calculation. A synthetic seismogram was added to a long period noise segment (from LASA), with the peak signal and noise amplitudes being equal. Comparing to the $\hat{M}_s$ calculation for the synthetic itself, the 20 second arrival time error is 4 seconds and the $\hat{M}_s$ error is 0.06. This and similar calculations done with a "perfect" estimate for the dispersion of the expected signal, show that the $\hat{M}_s$ algorithm works very well. Testing with real data where the prespecified dispersion is only approximately correct has not yet been done. However, we point out that the $\hat{M}_s$ calculation only requires an accurate identification of the MARS spectrum in a narrow period band, in this case near 20 seconds.

5.2.6 Conclusions

The automated magnitude algorithms appear to give consistent and convenient results, though much more extensive testing with real data is required. The $\hat{m}_b$ and $\hat{M}_s$ values may be viewed as a by-product of signal processing with the MARS
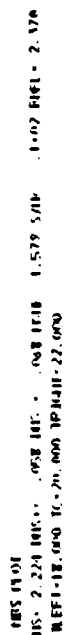
70

t_g (20 sec) = 507.6

Peak S/N = 1

Figure 34. Calculation of $\hat{M}_S$ for a seismogram with peak synthetic/peak noise = 1. The reference dispersion was that of the synthetic seismogram.

71
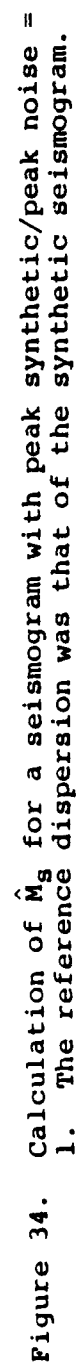
program, which is also configured for signal detection and
earthquake/explosion discrimination. Thus, these values can
easily be catalogued when processing data with MARS for other
purposes.

72

VI. GROUND MOTION ANALYSIS

6.1   INTRODUCTION

Task 4.5 involved a compilation and assessment of near
source data recorded from underground explosions with the pur-
pose of determining their significance for the definition of
nuclear source functions for different emplacement media. More
specifically, previously unpublished data from the Sandia
Corporation archives are being reviewed and integrated into
the previously compiled data base.

Work on this task was the topic of a report by Murphy
and Bennett (1980) and was described by Bache, et al. (1980a).
A summary is provided in the following subsection.

6.2   ANALYSIS OF FREE-FIELD DATA FROM EXPLOSIONS IN WET
TUFF AND ALLUVIUM EMPLACEMENT MEDIA BY J. R. MURPHY
AND T. J. BENNETT

Table 2 lists the events for which previously unpub-
lished free-field data have been collected. It can be seen
that data from eleven different explosions covering a yield
range from about 1 to 1200 KT are being investigated. These
events were detonated in wet tuff/rhyolite and alluvium emplace-
ment media and the associated depths of burial vary by more than
a factor of six. These data, together with those previously
collected, are being used to assess the dependence of seismic
coupling on source medium. For example, Figure 35 shows a
comparison of the reduced displacement potentials (RDP's) pre-
dicted using an analytical model based on Pahute Mesa explo-
sions in wet tuff/rhyolite with several observed RDP's from
Yucca Flat events in wet tuff. It can be seen that the pre-
dicted and observed agree fairly well, which suggests that
the seismic coupling properties of Yucca Flat tuff are similar
to those of the Pahute Mesa volcanics. However, a very different

73

TABLE 2

NUCLEAR EXPLOSIONS FOR WHICH PREVIOUSLY UNPUBLISHED
FREE-FIELD DATA HAVE BEEN COLLECTED

EVENT	MEDIUM	YIELD	DEPTH
AGILE	Wet Tuff	L-I	732 m
BOXCAR	Wet Rhyolite	1200 KT	1165 m
CALABASH	Wet Tuff	110 KT	626 m
CARPETBAG	Wet Tuff	220 KT	663 m
COMMODORE	Wet Tuff	250 KT	749 m
CYPRESS	Wet Tuff	L	411 m
DIESEL TRAIN	Wet Tuff	L	419 m
FAULTLESS	Wet Tuff	I	975 m
HUTCH	Wet Tuff	I	549 m
LANPHER	Wet Tuff	L-I	714 m
PLATTE	Tuff	1.85 KT	191 m

74

Figure 35. Comparison of observed tuff RDP's with RDP's predicted for the same yield and depth of burial in a wet tuff/rhyolite emplacement medium.

75

picture emerges when this same procedure is applied to explosions in dry Yucca Flat alluvium. Figure 36 shows a comparison of the observed RDP's from four events in dry alluvium with the corresponding RDP's predicted for the same yields and depths of burial in wet tuff/rhyolite emplacement media. It can be seen that these data clearly indicate that dry alluvium is a weak coupling medium with respect to wet tuff/ rhyolite, in agreement with the observed differences in the teleseismic m_b data from explosions in these two media. Thus, the available free-field data are essentially consistent with the teleseismic m_b data and, consequently, should be of use in their interpretation.
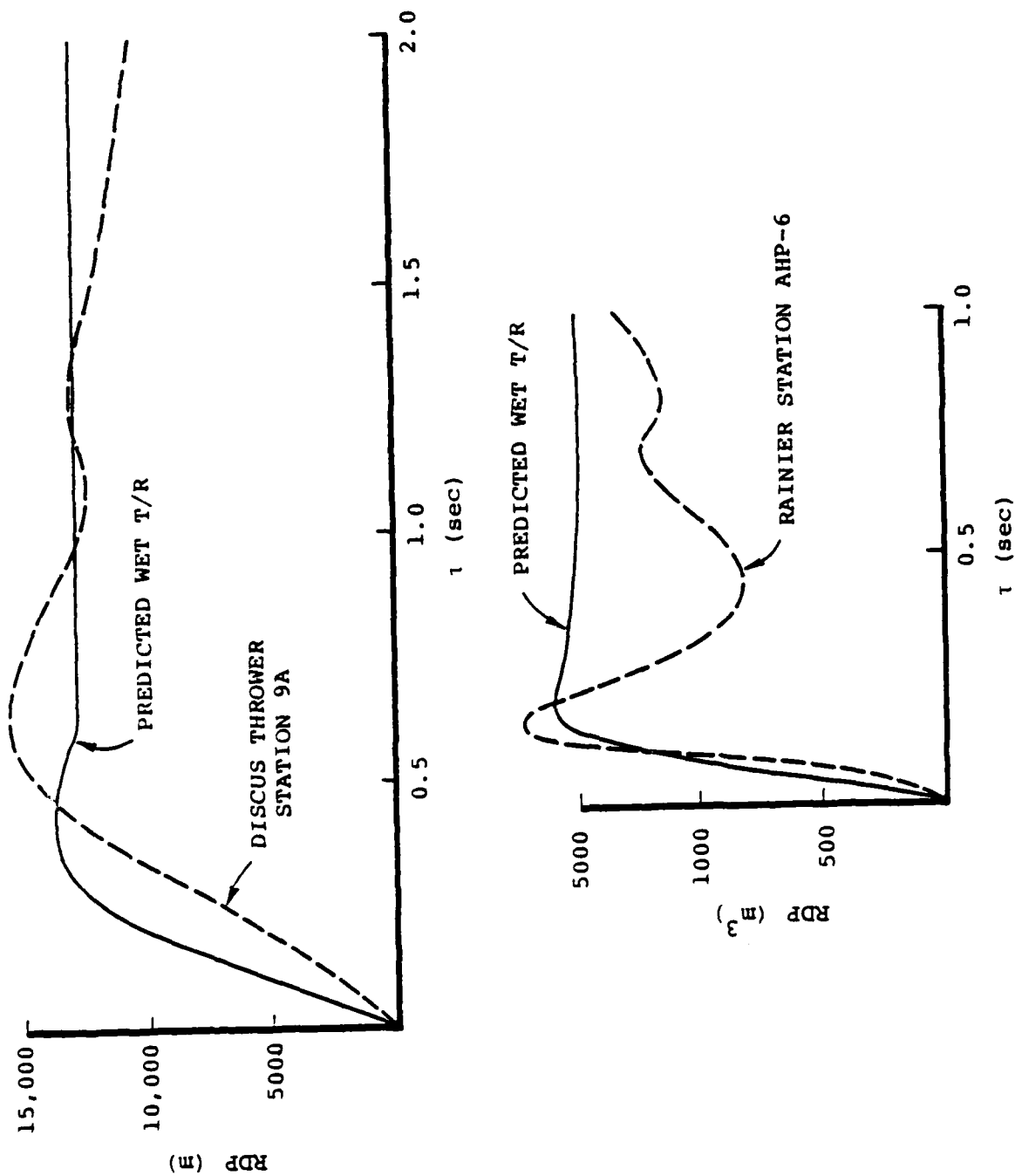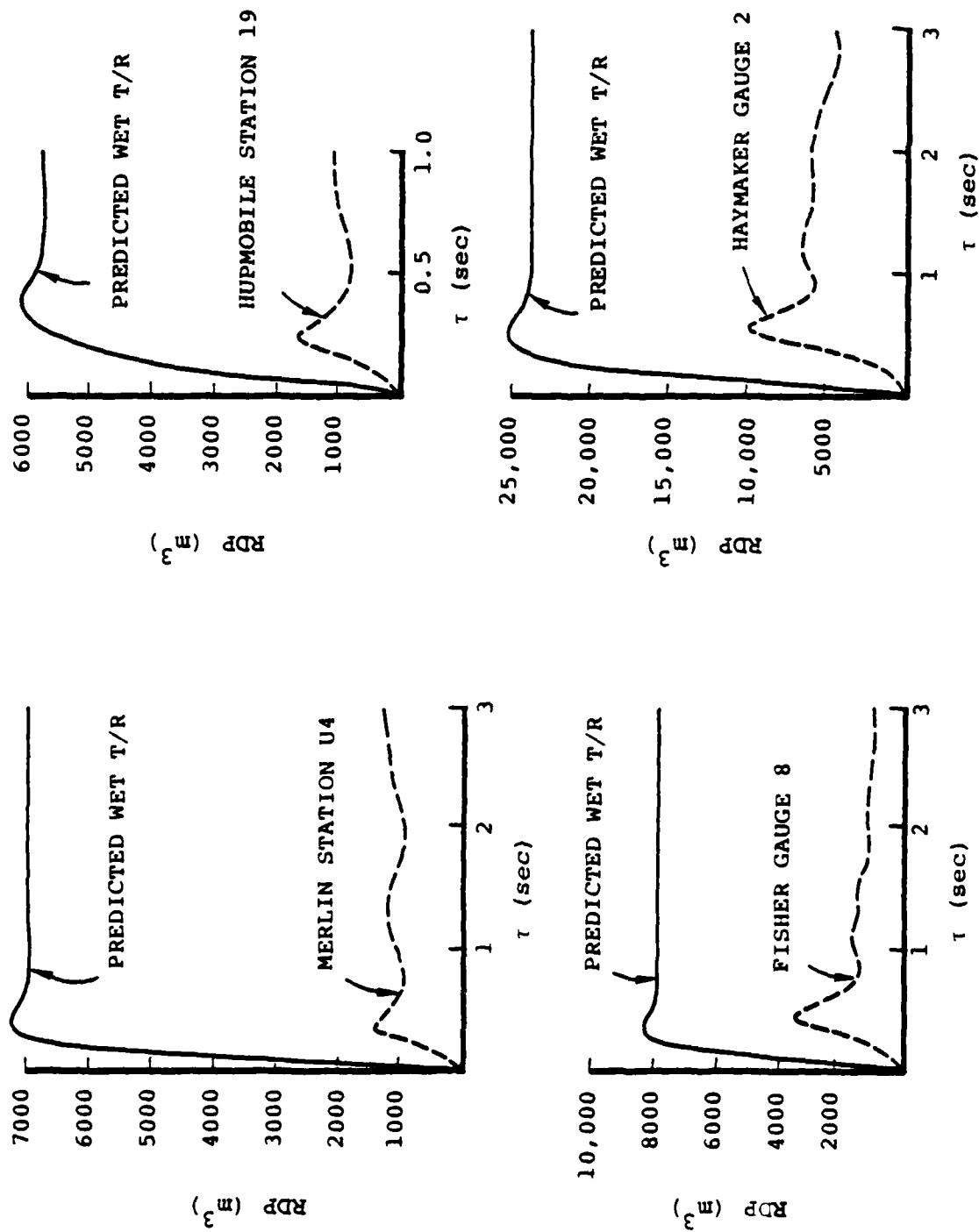
Figure 36. Comparison of observed alluvium RDP's with RDP's predicted for the same yield and depth of burial in a wet tuff/rhyolite emplacement medium.

77

VII.   ACOUSTIC WAVES FROM EXPLOSIONS IN THE OCEAN

7.1   INTRODUCTION

The study of the acoustic signature of a near surface oceanic explosion gave rise to a report by Bache, et al. (1980c). An executive summary of the results is included below.

7.2   THE UNDERWATER ACOUSTIC SIGNATURE OF A NUCLEAR EXPLOSION AT THE OCEAN SURFACE BY T. C. BACHE, T. G. BARKER, M. G. BROWN, K. D. PYATT AND H. J. SWANGER

7.2.1   Objective

The objective of this task is to estimate the gross spectral character and duration of the acoustic wave signature of a nuclear explosion near the ocean surface. The explosion is assumed to have a yield of 1 KT and the nominal range is 6600 km.

7.2.2   Accomplishments

The main results of this work are summarized in a report by Bache, et al. (1980). The technique was to construct theoretical pressure-time histories by convolving an elastic representation for the source with a Green's function representing the propagation. The source may include two parts. The first is the airblast loading applied to the surface and the second is the direct coupling of energy into the water. When the explosion is above a certain height, estimated to be 2.3 meters for 1 KT, the direct coupling contribution may be ignored. Thus, the calculations include the cases when the explosion is on or above the surface, though no attempt is made to account for height-of-burst effects that

78

may become important when the (1 KT) explosion is more than 10 meters above the surface.

Both components of the source are expressed in terms of pressure-time histories, $P(r,t)$ applied to the ocean surface. The total force applied is

$$\hat{F}(\omega) = \int_0^\infty P(r,\omega) \, J_0(\omega p r) \, r dr \ . \qquad (3)$$

The spectral amplitudes of the total force for both components of the source are plotted in Figure 37 for the ray parameter ($p = 0.667$ sec/km) appropriate for large distances.

The pressure at the receiver is obtained by convolving $\hat{F}(\omega)$ with the appropriate Green's function, which is the pressure at the receiver due to a vertical point load applied at the center of the source region. The Green's functions were computed with the WKBJ seismogram method (Chapman, 1978; Brown, et al., 1980). The results turned out to be very little different from those from geometric ray theory. Then for any particular ray arrival, the spectral pressure at the receiver is approximately

$$\hat{P}_r(\omega) \approx i \, \omega \, \hat{F}(\omega) \cdot Q(\omega) \ , \qquad (4)$$

where $Q(\omega)$ represents the frequency-dependent filter imposed by the travel path. However, at the frequencies of interest (< 50 Hz), absorption in the ocean is very small. Therefore, we assume that $Q(\omega) = 1$. The total record is a summation of many rays, leading to a total spectrum which is merely a modulated version of Equation (4).

In Figure 38, we plot our estimates for the spectra of the pressure pulse at a hydrophone in the deep ocean at a large distance from the explosion. The direct coupling

79
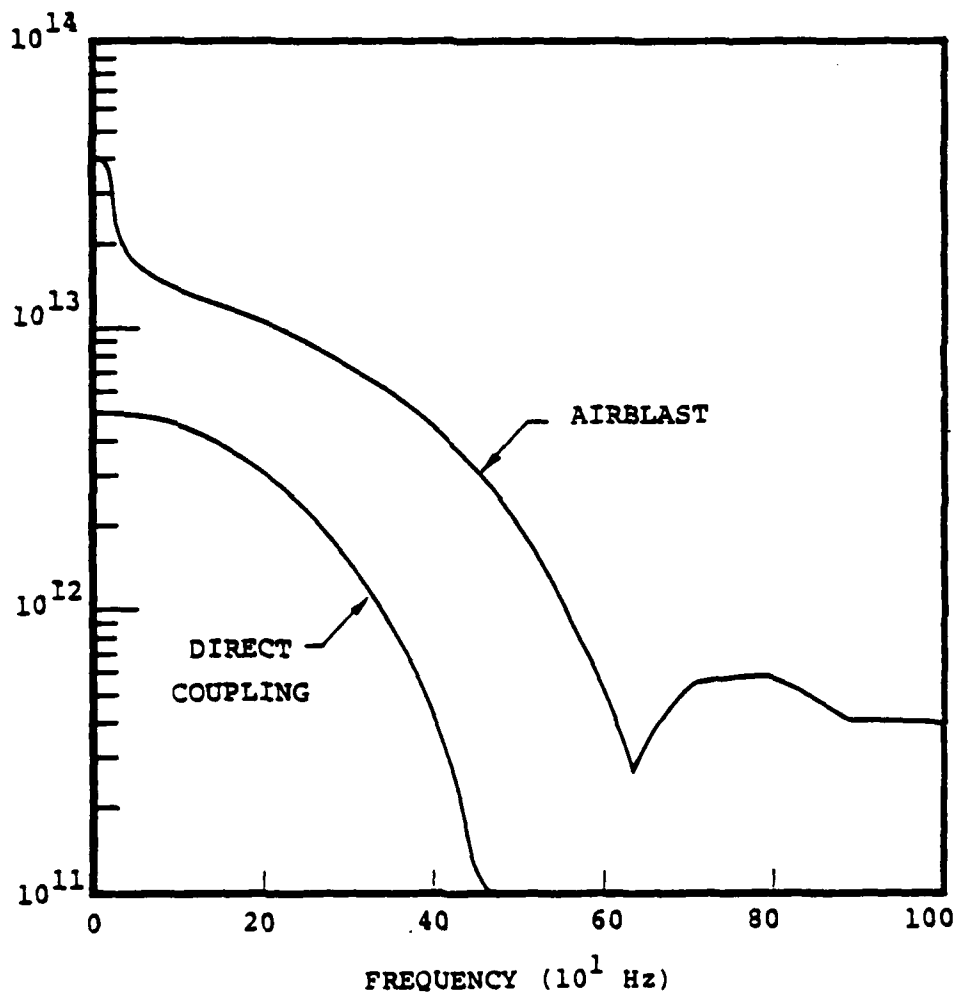
Figure 37. The explosion source spectra.

80
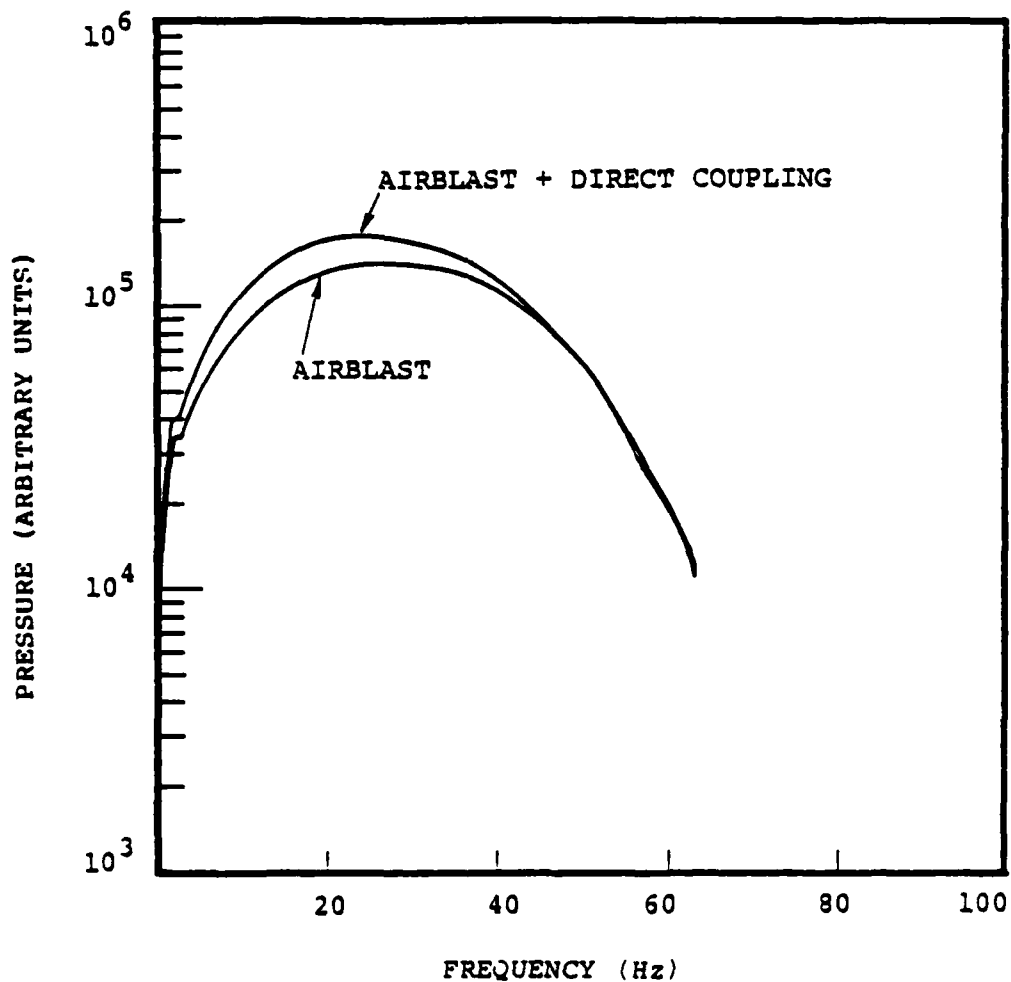
Figure 38.   The spectrum of the pressure time history of a single
             ray arrival at a SOFAR axis receiver station. The
             complete signal spectrum, which is a sum of many single
             ray spectra, would have the same basic shape. The
             amplitude units are arbitrary, depending on the amplitude
             of the Green's function for the travel path.

81

contribution is small and the spectrum is band-limited, having a peak near 22 Hz and being down by a factor of 3 from the peak at about 4 and 50 Hz. The spectra cube-root scale with yield. That is, if the yield were 2 KT, the spectrum in Figure 38 shifts to frequencies smaller by a factor of 1.26.

To estimate the signal duration, the Green's functions were computed with WKBJ seismogram theory for a variety of assumptions about the ocean sound velocity profile. At the large ranges (> 3500 km) of interest, the main contribution is from rays that turn above the ocean bottom. For a reflection coefficient of as large as 0.98, the bottom bounces make almost no contribution because they reflect so many times.

The calculated signal duration varies widely, depending upon the assumptions about the sound velocity profile. Values from 20 to 60 seconds seem most reasonable for a range of about 6600 km. The duration scales directly with range.

REFERENCES

Allen, R. V. (1978), "Automatic Earthquake Recognition and Timing from Single Traces," BSSA, 68, pp. 1521-1532.

Bache, T. C. (1979), "$\hat{m}_b$, a Spectral Body Wave Magnitude (U)," Systems, Science and Software Report SSS-CR-79-3901 submitted to AFTAC/VSC, January.

Bache, T. C., S. M. Day and J. M. Savino (1979), "Automated Magnitude Measures, Earthquake Source Modeling, VFM Discriminant Testing and Summary of Current Research," Systems, Science and Software Quarterly Technical Report SSS-R-79-3933 submitted to AFTAC/VSC, February.

Bache, T. C., J. Murphy, S. M. Day, T. J. Bennett and B. Shkoller (1980a), "Regional Detection of Decoupled Explosions, Yield Estimation from Surface Waves, Two-Dimensional Source Effects, Three-Dimensional Earthquake Modeling and Automated Magnitude Measures," Systems, Science and Software's Semi-Annual Technical Report SSS-R-80-4594 submitted to Advanced Research Projects Agency, July.

Bache, T. C., T. G. Barker, N. Rimer and J. T. Cherry (1980b), "Contribution of Two-Dimensional Source Effects to the Far-Field Seismic Signatures of Underground Nuclear Explosions," Systems, Science and Software Topical Report SSS-R-80-4569 submitted to ARPA/VSC, July.

Bache, T. C., T. G. Barker, M. G. Brown, K. D. Pyatt, and H. J. Swanger (1980c), "The Underwater Acoustic Signature of a Nuclear Explosion at the Ocean Surface," Systems, Science and Software Interim Technical Report SSS-R-80-4586 submitted to AFTAC/VSC, July.

Bache, T. C., J. R. Murphy and S. M. Day (1980d), "Regional Detection of Decoupled Explosions, Yield Estimation from Surface Waves, Two-Dimensional Source Effects, Three-Dimensional Earthquake Modeling and Automated Magnitude Measures," Systems, Science and Software Semi-Annual Technical report SSS-R-80-4594 submitted to AFTAC/VSC, July.

Berger, J. (1980), "Seismic Detectors: The State-of-the-Art," Systems, Science and Software Technical Report SSS-R-80-4588 submitted to AFTAC/VSC, July.

Brown, M. G., W. H. Munk, J. L. Spiesberger and P. F. Worcester (1980), "Long-Range Acoustic Transmission in the Northwest Atlantic," JGR, 85, pp. 2699-2703.

Chapman, C. H. (1978), "A New Method for Computing Synthetic Seismograms," _Geophys. J._, 54, pp. 481-518.

Farrell, W. E., J. Wang, C. B. Archambeau and R. Goff (1980), "Evaluation of the Mars Seismic Event Detector," Systems, Science and Software Technical Report SSS-R-81-4656 submitted to Advanced Research Projects Agency, August.

Filson, J. and H. Bungum (1972), "Initial Discrimination Results from the Norwegian Seismic Array," _Geophy. J._, 31, pp. 315-328

Frieberger, W. F. (1963), "An Approximate Method in Signal Detection," _Quarterly Appl. Math._, 20, pp. 373-378.

Hadley, D. M. and R. S. Hart (1979), "Seismic Studies of the Nevada Test Site," Sierra Geophysics Quarterly Tehcnical Report submitted to VSC/ARPA, SGI-R-79003, June.

Jordan, H. N., W. V. Mickey, W. Helterbran and D. W. Clark (1966), "Travel Times and Amplitudes from the SALMON Explosion," _JGR_, 71, No. 14.

Masso, J. F., C. B. Archambeau and J. M. Savino (1979), "Implementation, Testing and Specification of a Seismic Event Detection and Discrimination System," Systems, Science and Software Final Report SSS-R-79-3963 submitted to ACDA, March.

Mueller, R. A., and J. R. Murphy (1971), "Seismic Characteristics of Underground Nuclear Detonations Part I: Seismic Spectrum Scaling," _BSSA_, 67, pp. 1675-1692.

Murphy, J. R. and T. J. Bennett (1980), "A Simulation Study of the Detectability of a 5.3 KT Decoupled Explosion at Regional Distances in Eastern United States," Technical Memo to Major G. Wayne Ullrich, VSC, May 6, 1980.

Murphy, J. R. (1977), "Seismic Source Functions and Magnitude Determinations for Underground Nuclear Detonations," _BSSA_, 67, No. 1.

Perl, N., F. J. Thomas, J. Trulio and W. L. Woodie (1979), "Effect of Burial Depth on Seismic Signals, Volume I," Pacific Sierra Research Technical Report submitted to DNA/ARPA, PSR Report 815, May.

Perl, N. and J. Trulio (1979), "Effect of Burial Depth on Seismic Signals, Volume II," Pacific Sierra Research Technical Report submitted to DNA/ARPA, PSR Report 815, May.

Rimer, N., J. T. Cherry, S. M. Day, T. C. Bache, J. R. Murphy and A. Maewal (1979), "Two-Dimensional Calculation of PILEDRIVER, Analytic Continuation of Finite Difference Source Calculations, Analysis of Free Field Data from MERLIN and Summary of Current Research," Systems, Science and Software Quarterly Technical Report SSS-R-79-4121 submitted to VSC/ARPA.

Rivers, W. and D. H. von Seggern (1979), "Effect of Tectonic Strain Release on Surface-Wave Magnitudes," to be published as Teledyne Geotech Technical Report SDAC-TR-79-6 submitted to VSC/ARPA.

Savino, J. M., C. B. Archambeau and J. F. Masso (1980), "Discrimination Results from the Priority 2 Stations," Systems, Science and Software Technical Report SSS-R-80-4566 submitted to AFTAC/VSC, July.

Springer, D., M. Denny, J. Healy, and W. Mickey (1968), "The Sterling Experiment: Decoupling of Seismic Waves by a Shot-Generated Cavity," JGR, 73, (18), pp. 5995-6010.

Unger, R. T. (1978), "Automatic Detection, Timing and Preliminary Discrimination of Seismic Signals with the Instantaneous Amplitude, Phase and Frequency," Texas Instruments Report no ALEX(01)-TR-77-04, AFTAC Contract No. F08606-77-C-0004, Texas Instruments, Incorporated, Dallas, Texas.